A DOCTORAL DISSERTATION

Electrical Impedance Sensors for Volume Fraction Measurements of Two-Phase Flows

Department of Nuclear & Energy Engineering

GRADUATE SCHOOL

JEJU NATIONAL UNIVERSITY

Min Seok Ko

February, 2014

博士學位論文

이상유동 부피분율 측정을 위한 전기 임피던스 센서

濟州大學校 大學院

에 너 지 工 學 科

高 敏 碩

2014年 2月

이상유동 부피분율 측정을 위한
전기 임피던스 센서

指導敎授 金 信

高 敏 碩

이 論文을 工學博士學位論文으로 提出함

2014年 2月

高敏碩의 工學 博士學位 論文을 認准함

審査委員長 朴 在 雨 (인)

副委員長 金 信 (인)

委 員 金 慶 淵 (인)

委 員 金 南 鎭 (인)

委 員 尹 炳 祚 (인)

濟州大學校 大學院

2014年 2月

Electrical Impedance Sensors for Volume Fraction Measurements of Two-Phase Flows

Min Seok Ko
(Supervised by professor Sin Kim)

A thesis submitted in partial fulfillment of the requirement for the degree of Doctor of Nuclear and Energy Engineering.

2014. 2.

This thesis has been examined and approved.

.....
Thesis director, Jae-Woo Park, Professor, Department of Nuclear & Energy Engineering

.....
Thesis vice director, Sin Kim, Professor, Department of Nuclear & Energy Engineering

.....
Kyung-Youn Kim, Professor, Department of Electronic Engineering

.....
Nam-Jin Kim, Professor, Department of Nuclear & Energy Engineering

.....
Byong-Jo Yun, Professor, Department of Mechanical Engineering

(Name and signature)

2014. 2.
Date

Department of Nuclear & Energy Engineering
GRADUATE SCHOOL
JEJU NATIONAL UNIVERSITY

Contents

List of Figures

List of Tables

Abstract

Two-phase flows are frequently encountered phenomena in various engineering fields such as chemical, oil and nuclear industries. In particular, the volume fraction in two-phase flow systems has very important roles in determining several variables associated with system analyses and design like the two-phase mixture density and viscosity, average velocity of two phases, pressure drop, and heat transfer. For this reason, a very wide variety of techniques including the quick-closing valve, gamma or X-ray absorption, optical probe, and electrical impedance have been proposed for volume fraction measurement. Among these, in particular, the electrical impedance technique has various favorable characteristics in terms of easy implementation, relatively low construction cost, fast data acquisition speed, no intrusiveness of flow fields, and convenient mobility.

The electrical impedance technique is based on the fact that two phases have different electrical properties. In the electrical impedance technique, in general, voltages or currents are applied to electrode pairs installed in a test section and resultant electrical resistance and/or capacitance measurement is directly used to estimate the volume fraction.

In volume fraction measurement based on the electrical impedance, electrode and gap sizes of an impedance sensor are the most important design parameters because the electric field distribution having significant influences on the electrical impedance directly depends on them. The non-uniformity of the electric field due to an improper sensor configuration causes undesirable impedance sensor characteristics such as a nonlinear response for the volume fraction.

The present work considers this dependence of electrical signals on the sensor configuration and focuses on designing the impedance sensor providing favorable

characteristics for volume fraction or film thickness measurement. For this, two conventional sensor configurations (plate- and ring-type sensors) and separated flow patterns (stratified and annular flow) are taken into account. For an annular flow application, gas core fluctuations which can distort output signals are considered as a key design parameter and the optimal sensor gap sizes, which give stable void fraction measurement without being affected by the gas core fluctuations, are determined for both plate- and ring-sensor types. Similarly, in a stratified flow example the electrode and gap sizes of a ring-type impedance sensor are optimized in view of the sensor linearity for liquid film thickness changes. In addition, as another application, a conductance sensor is applied for flow regime classification in an inclined pipe and its signal characteristics for various flow rate conditions which cover stratified, intermittent and annular flows are investigated.

1. Introduction

1.1. Definition of volume fraction

The fraction of the control volume V which is occupied by the phase k at a given time can be expressed as

$$\alpha_k = \frac{1}{V}\iiint_V \beta_k dV = \frac{V_k}{V}, \tag{1.1}$$

where β_k is the phase density function which corresponds to 1 when a certain position is occupied by the phase k, otherwise is equal to 0. The volume fraction of the gaseous phase is generally referred to as the *void fraction* and is written by

$$\alpha_g \equiv \alpha = \frac{V_g}{V}, \tag{1.2}$$

where the subscript 'g' is often omitted. Similarly, $1-\alpha$ or α_ℓ is referred to as the *liquid fraction*.

In most practical situations, two-phase flows are sufficiently turbulent to make α_k to fluctuate even for steady-state flow conditions. For this situation, the time-averaged value is usefully introduced. The time-averaged volume fraction for the phase k is defined as

$$\tilde{\alpha}_k = \frac{1}{\Delta t}\int_{t-\Delta t/2}^{t+\Delta t/2} \alpha_k \, dt, \tag{1.3}$$

where Δt is the measurement time.

1.2. Volume fraction measurement techniques

The volume fraction is a key parameter to characterize two-phase flow patterns and to determine several variables including the two-phase mixture density and viscosity, average velocity of two phases, pressure drop, and heat transfer. Therefore, accurate measurement for the volume fraction is essential for system analyses and design.

For this reason, various volume fraction measurement techniques have been proposed. Among them, in particular, the quick-closing valve technique has been most commonly used over the past several decades. In the quick-closing valve technique, valves are placed at each end of the test section where the volume fraction is to be measured. The valves are quickly closed to isolate the test section. Then, the liquid phase is drained out and its volume is determined. It is advantageous in simple implementation; however, it has of course significant limitations in real-time and local measurement. Due to these weaknesses, it has been mainly used to develop void fraction correlations and to calibrate other void fraction measurement instruments (Woldesemayat and Ghajar 2007, Rosa *et al.* 2012, Zhao *et al.* 2013).

The volume fraction measurement techniques based on nuclear sources have been also widely used (Å bro and Johansen 1999, Kendoush and Sarkis 2002, Stahl and Rudolf von Rohr 2004). In the gamma or X-ray absorption technique, a beam of gamma or X-rays is attenuated by absorption and scattering according to the exponential absorption equation as a function of the linear absorption coefficient and the travel distance through the absorbing medium. For volume fraction measurement, in general, the calibration to determine the received intensities for the test section full of the gas and liquid phase is first conducted. Then, a intensity for a certain gas-liquid two-phase flow is evaluated. Finally, the volume fraction is

measured using the logarithmic or linear relationship between the measured intensities and the volume fractions. Although widely applied, safety problems due to radiation and relatively high construction cost are its main drawbacks.

The electrical impedance technique has also received many attentions (Paranjape *et al.* 2012, Schlegel *et al.* 2014). In this technique, one or more pairs of electrodes are installed inside or outside of the pipe wall and measure the resistance and/or the capacitance between these electrode pairs. From the calibration curve between the measured signal and the volume fraction, the measured resistance and/or capacitance data is converted into the volume fraction. Due to the dependence of the electrical signal on flow patterns, separated calibration curves are needed (Rosa *et al.* 2012, De Kerpel *et al.* 2013).

A tomographic method such as electrical impedance tomography (EIT) does not require any prior information on the flow patterns unlike the electrical impedance technique, but poor spatial and temporal resolutions are main drawbacks. A wire-mesh sensor, the other tomographic method, visualizes two-phase flows at a relatively good temporal resolution because measured current data are directly converted into the phasic volume; however, the intrusiveness of the flow field due to its own structure is a significant weakness (Prasser *et al.* 1998).

Compared to others, the electrical impedance technique has various favorable features. Firstly, it is cost-efficient. According to the Ovacik and Jones' report (1998), the construction cost for the electrical impedance technique was assessed to be about 10 times cheaper than the gamma or X-ray absorption technique. Secondly, the measurement speed is sufficiently fast so that it is normally utilized for two-phase flows. Recently, Olerni *et al.* (2013) measured the distribution of the void fraction at a time resolution of roughly 900 frame per second using an electrical resistance tomography (ERT) system equipped with 16

sensing electrodes. Thirdly, it does not disturb the flow field. In addition, it is advantageous in mobility and emitting no radiation.

Owing to these merits of the electrical impedance technique, various researches have been performed. In the next section, a more detailed literature survey for the electrical impedance technique is presented.

1.3. Electrical impedance techniques for volume fraction measurement

Researches on the electrical impedance technique are mainly classified into a capacitance or conductance method and for each method various sensor geometries have been proposed. One of the most typical types is a plate-type sensor. In this configuration, one or more pairs of concave electrodes are attached on the inner or outer wall of the pipe and the electrode pairs usually face each other (Shu *et al.* 1982, Kendoush and Sarkis 1995, Lowe and Rezkallah 1999, Ahmed 2006, Canière *et al.* 2008, Kim *et al.* 2009b, Strazza *et al.* 2011, De Kerpel *et al.* 2013). A ring-type sensor is another typical one. For the ring-type sensor, two or more ring electrodes covering the whole pipe circumference are arranged along the pipe (Andreussi *et al.* 1988, Tsochatzidis *et al.* 1992, Kendoush and Sarkis 1995 Fossa 1998, Ahmed 2006, Kim *et al.* 2009a, Rosa *et al.* 2012). Other types include helical (Geraets and Borst 1988, Ye *et al.* 2011), internal sensors (Yang *et al.* 2003) and a modified ring-type sensor with non-uniform electrode and gap sizes (Devia and Fossa 2003).

Although the forementioned publications have adopted similar sensor types one another, their research targets have been somewhat different in view of the sensor design. Some of them have focused on the sensor linearity for pipe thicknesses (Shu *et al.* 1982, Geraets and Borst 1988) and for separation distances (Andreussi *et al.* 1988, Devia and Fossa

2003). Meanwhile, some have designed the impedance sensor in terms of the sensitivity and the edge effect (Song *et al.* 1998, Lowe and Rezkallah 1999, Ahmed 2006, Canière *et al.* 2008, Strazza *et al.* 2011). More recent publications have proposed a sensor arrangement to reduce the effect of working fluid temperature on impedance measurement (Kim *et al.* 2009a) and methodologies to reflect the dependence of the electrical impedance on the flow patterns for volume fraction measurement (Rosa *et al.* 2012, De Kerpel *et al.* 2013).

1.4. Objective and outline

The present work has been initiated to design the impedance sensor for volume fraction or film thickness measurement in two-phase flows. The major characteristics that the impedance sensor should have in the practical two-phase flows would be the linearity between the impedance (resistance and/or capacitance) and the volume fraction or the liquid film thickness. However, most of previous studies have concentrated on only the performance of various sensors with fixed sensor dimensions determined by researcher's experience or simplified theories such as the equivalent circuit theory, not by systematic analyses (Abouelwafa and Kendall 1980, Kendoush and Sakis 1995, Fossa 1998, Strazza *et al.* 2011). Although some of them have attempted theoretical treatments for the sensor design, they considered simplified geometries like concentric annular flow and two-dimensional electric field (Shu *et al.* 1982, Tsochatzidis *et al.* 1992, Andreussi *et al.* 1988) or proposed a complicated sensor configuration compared to the conventional sensors (Devia and Fossa 2003).

To achieve the purpose, this thesis considers two common sensor types easy to implement (plate- and ring-type sensors) and model flows (stratified and annular flow). For

each sensor and flow pattern, systematic numerical calculations are performed to design the impedance sensor generating favorable characteristics and experiments to verify the sensor design are conducted. In addition, electrical signal characteristics for some flow patterns observed in an inclined pipe are investigated.

This thesis mainly consists of 6 chapters. In Chapter 2, the governing equation for the impedance technique and some important parameters to be considered are presented. In Chapter 3, as an application example, gas-liquid two-phase annular flows are considered and the optimal electrode gap sizes, which give reliable void fraction measurement irrespective of gas core locations in the annular flows, are numerically determined for both plate- and ring-sensor types. Also, the optimized sensor gap sizes are verified by comparison experiments. In Chapter 4, similarly, the electrode and gap sizes of a ring-type impedance sensor are optimized in view of the linearity between the electrical impedance and the liquid film thickness in gas-liquid two-phase stratified flows. In addition, the optimized sensor is applied for loop experiments and its performance is evaluated in comparison with the measurement results from a high-speed camera. In Chapter 5, some statistical parameters obtained from measured conductance signals are analyzed for various flow rate conditions which cover stratified, intermittent and annular flows in an inclined pipe. Finally, in the last chapter, concluding remarks are presented.

2. Theoretical background for electrical impedance technique

2.1. Governing equation

The governing equation for conductive or dielectric medium can be derived from the Maxwell's equations. That is, the electrical potential distribution can be described by the following Laplace equation with proper boundary conditions.

$$\nabla \cdot (\sigma + i\omega\varepsilon)\nabla\phi = 0, \tag{2.1}$$

where σ and ε are the electrical conductivity and permittivity equal to $\varepsilon_r\varepsilon_0$, respectively. Here, ε_r and ε_0 represent the relative permittivity for an arbitrary medium and permittivity value for vacuum ($\varepsilon_0 = 8.854 \times 10^{-12} F/m$), respectively. Also, in above equation *i* is the imaginary unit and ω is the angular frequency equal to $2\pi f$, here f is the signal frequency. The potential distribution to be determined is ϕ.

In Eq. (2.1), when the conductivity component is much more dominant than the permittivity term ($\sigma \gg \omega\varepsilon$), the reactance contribution to the electrical impedance becomes negligible and the governing equation is reduced to $\nabla \cdot \sigma\nabla\phi = 0$, which is often referred to as the *conductance method*. On the other hand, in the case the permittivity term is much larger than the conductivity ($\sigma \ll \omega\varepsilon$), the resistance contribution to the impedance becomes smaller and the governing equation is simplified to $\nabla \cdot \varepsilon\nabla\phi = 0$, which is referred to as the *capacitance method*.

2.2. Electrical impedance and admittance

The electrical impedance is a measure of the opposition to an electrical current when a voltage is applied. It is the complex ratio of the applied voltage to the current which can be obtained from the solution to the Laplace equation (2.1). That is, $Z = \Delta V / I = R + iX$ where Z, ΔV and I represent the electrical impedance, applied voltage difference and electrical current, respectively. The resistance R is the real part of the impedance, which is given by $R = |Z| \cos\theta_{\text{pha}}$. Similarly, the reactance X is the imaginary part of the impedance corresponding to $X = |Z| \sin\theta_{\text{pha}}$. Here, $|Z|$ is the magnitude of the impedance equal to $|Z| = \sqrt{R^2 + X^2}$ and θ_{pha} is the phase angle given by $\theta_{\text{pha}} = \tan^{-1}(X / R)$. The reactance in the electrical impedance is separated into the capacitive X_C and inductive reactance X_L. The former is inversely proportional to the signal frequency that is, $X_C = 1/\omega C$, while the latter is in direct proportion to the signal frequency $X_L = \omega L$. In these relations, C and L denote the capacitance and the inductance, respectively. The total reactance is given by $X = X_L - X_C$.

In contrast with the impedance, the electrical admittance is a measure of how easily a circuit allows the current to flow and quantitatively defined as the inverse of the impedance. That is, $Y = 1/Z = G + jB$. Here, G is the electrical conductance given by $G = R/(R^2 + X^2)$ and B is the susceptance defined as $B = -X/(R^2 + X^2)$.

2.3. Parameters having influences on electrical signal

2.3.1. Flow pattern

The flow pattern or regime, in general, differently appears according to physical properties of working fluids, relative velocities of two phases, orientations of fluids, and channel configurations. Typically, bubbly flows tend to form for high liquid flow rates irrespective of experimental conditions and set-up. As the gas flow rate increases, the bubbly flows start developing to slug or plug flows due to bubble coalescences. Further increase of the gas flow rate gives rise to the formation of the gas core covering almost entire pipe cross-section. Figures 2.1 and 2.2 show photographs for some typical flow regimes observed in a vertical and near-horizontal pipe, respectively.

From the viewpoint of the electrical impedance technique, this phase distribution is treated as the electrical property distribution of the two phases. In the case of gas-liquid two-phase stratified flows where the electrical conductivity and permittivity values of the gas phase are negligibly small, the electrical current may flow through the conductive or dielectric liquid film on the bottom (Fig. 2.1); on the other hand, for annular flows the non-conductive gas core bridges the current path and as a result the electrical current flows through the liquid film distributed around the wall of the pipe (Figs. 2.1 and 2.2). In the annular cases, of course, the effect of the electric field near the sensor gap on electrical signals may be more significant than stratified flow structures. These different dependences of the electrical current on flow structures lead to different impedance measurement and consequently different volume fraction measurement. Therefore, prior information on the flow patterns should be given for volume fraction measurement based on the electrical impedance.

It is well known that typical calibration curves for the electrical impedance and the volume fraction in stratified flows have S-shapes (Shu *et al.* 1982, Andreussi *et al.* 1988, Tsochatzidis *et al.* 1992, Fossa 1998, Devia and Fossa 2003, De Kerpel *et al.* 2013). For annular flows, on the other hand, the dimensionless impedance and the volume fraction curves typically show concave shapes (Shu *et al.* 1982, Kim *et al.* 2009b, De Kerpel *et al.* 2013).

The researches dealing with sensor responses for dispersed flow patterns have been scarcely performed. Most publications have adopted the classical equations by Maxwell and Bruggman for bubbly flows although Yang *et al.* (2003) tried to measure the space-averaged void fraction using Styrofoam spheres for simulating air bubbles. Instead, researches for local void fraction measurement using probes with small tips have been mainly carried out (Hibiki and Ishii 2000, Euh *et al.* 2001, Vejražka *et al.* 2010). The void fraction measurement based on wire-mesh sensor systems is also notable (Prasser *et al.* 2001, Prasser *et al.* 2005, Prasser 2007).

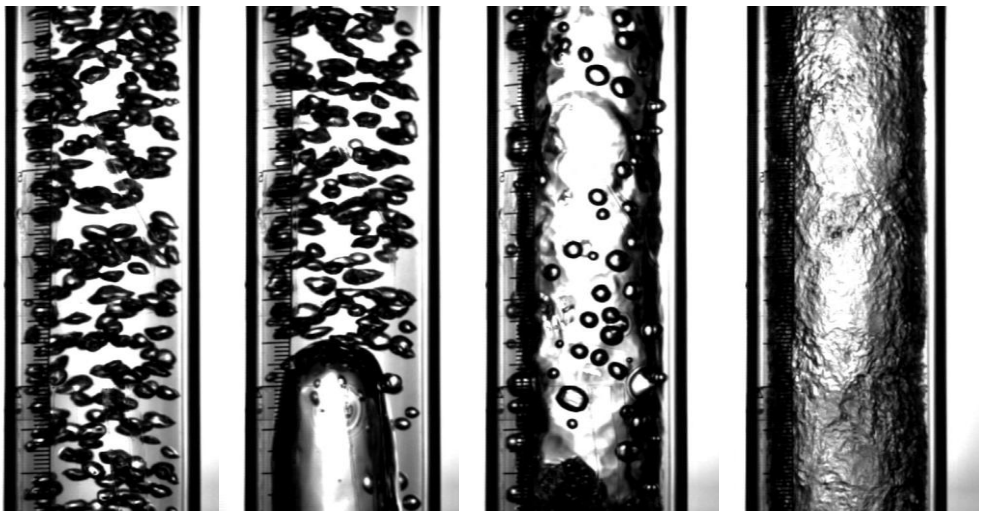

Figure 2.1. Some typical flow patterns in a vertical pipe
(bubbly, slug, churn and annular flow from the left).

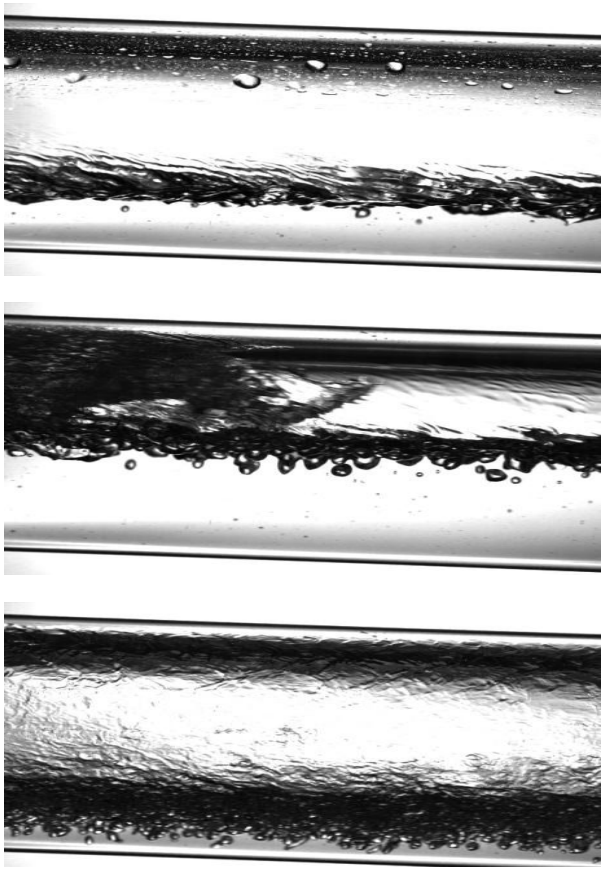

Figure 2.2. Some typical flow patterns in a near-horizontal pipe (stratified, slug and annular flow from the top).

2.3.2. Electrode and gap sizes

Besides the flow pattern, the electrode and gap sizes are also key design parameters to be considered because the electric field distribution inside the sensor is directly dependent on these variables. For a plate-type sensor with a small gap, for example, the distortion of the electric field occurs because the potential gradient near the gap is much steeper than other regions. As the gap size increases, this non-uniformity of the electric field distribution may be mitigated even though the edge effect can be another variable. These different characteristics of the electric field induced by different sensor arrangements determine the characteristic of the sensor response for the volume fraction or the liquid film thickness.

The publications demonstrating the effect of the electrode and gap sizes on the electrical impedance have been hardly found although some results for the sensor responses with respect to the electrode, gap, and pipe thickness in stratified and concentric annular flows have been reported (Sue *et al.* 1982, Andreussi *et al.* 1988, Geraets and Borst 1988, Devia and Fossa 2003).

2.4. Summary

In the first two sections the governing equation for the impedance technique and the physical definition of the electrical impedance were discussed. In the following section some parameters to be considered for the impedance technique were introduced. Besides these variables, the temperature of operating fluids (Kim *et al.* 2009a) and the contact impedance between electrode surfaces and fluid which were not presented in the text are other factors having influences on electrical signals.

It is the well-known fact that the electrical conductivity for water increases by 2 ~ 3% with an increase in temperature of 1° C and permittivity decreases by roughly 2% with an increase of 5° C for a temperature range 20 ~ 100° C. If the temperature is known, these changes of the electrical properties with the fluid temperature and their effects on impedance measurement can be compensated with an aid of the temperature and electrical conductivity or permittivity curves from material handbooks.

In general, the contact impedance has the particular importance when the imperfect contact spots between the solid interfaces exist and gases in the spaces created by the contact are present. For this case, the gases are regarded as the major impedance, which causes an additional voltage drop, because their electrical properties are very small. It has been mainly

dealt with in the applications of biomedical imaging where the imperfect contact surfaces between the human skins and the sensing electrodes exist (Hua *et al.* 1993).

As briefly mentioned above, the temperature effect is compensated by the calibration and the contact impedance may give a negligible effect in two-phase flow applications unlike in the applications dealing with solid to solid interfaces. The present work mainly consider the effect of the sensor geometry on the electrical impedance. The following two chapters (Chapters 3 and 4) introduce some numerical and experimental results to determine the sensor geometry for two given flow regimes.

3. Design of a capacitance sensor for void fraction measurements of air-water two-phase annular flows in vertical pipes

3.1. Problem description and numerical modeling

Figure 3.1 shows the schematic diagrams of an annular flow composed of the gas core in the center of the pipe and the liquid film around the wall of the pipe equipped with two different capacitance sensor types. Their permittivity values are given as ε_ℓ and ε_g, respectively, and they are assumed to be constant for the standard temperature and pressure. For a plate-type sensor, two identical concave electrodes ($\partial\Omega_{e1}$ and $\partial\Omega_{e2}$) are fitted to the inner wall of the pipe and these are separated by two gaps ($\partial\Omega_g$) with an angle δ. The radii of the gas core and the pipe are a and b, respectively. Similarly, in the case of a ring-type sensor two identical electrodes which occupy the whole circumference of the pipe and have a width of W_e are installed in the inner wall of the pipe with the radius b. These two ring electrodes are separated by a gap with a width W_g.

In each region, the potential distribution of ϕ_g and ϕ_ℓ satisfies the following Laplace equations:

$$\nabla \cdot \varepsilon_g \nabla \phi_g = 0 \quad \text{for gas core region } (0 \le r \le a), \tag{3.1}$$

$$\nabla \cdot \varepsilon_\ell \nabla \phi_\ell = 0 \quad \text{for liquid film region } (a \le r \le b), \tag{3.2}$$

where the subscripts 'g' and 'ℓ' denote the gas core and liquid film region, respectively. The governing equations are subjected to the following boundary conditions:

$$\phi_\ell = V_0 \quad \text{on } \partial\Omega_{e1}, \tag{3.3}$$

$$\phi_\ell = -V_0 \quad \text{on } \partial\Omega_{e2}, \tag{3.4}$$

$$\varepsilon_\ell \frac{\partial \phi_\ell}{\partial r} \quad \text{on } \partial\Omega_g, \tag{3.5}$$

$$\varepsilon_\ell \left.\frac{\partial \phi_\ell}{\partial r}\right|_{r=a} = \varepsilon_g \left.\frac{\partial \phi_g}{\partial r}\right|_{r=a}. \tag{3.6}$$

If the charge is written by Q, then from the definition of the capacitance C becomes $Q/2V_0$. Here, Q is evaluated from the charge density on the electrodes. For convenience, we introduce the dimensionless capacitance C^* as follows:

$$C^* = \frac{C - C_\ell}{C_g - C_\ell}, \tag{3.7}$$

where C is the capacitance response to an arbitrary void fraction α defined as

$$\alpha = \left(\frac{a}{b}\right)^2. \tag{3.8}$$

C_g and C_ℓ are the capacitance values for the sensors filled with only the gas ($\alpha = 1$) and liquid phases ($\alpha = 0$), respectively.

The capacitance response given in Eq. (3.8) is dependent on the void fraction, eccentricity of the gas core, and sensor arrangement. For reliable void fraction measurement based on capacitance signals in annular flows, the stable capacitance response which depends on only the void fraction without being affected by the gas core fluctuations is basically required. This work uses the fact that when the gap size between the electrodes changes, then the electric field distribution also changes and consequently this causes the sensor response to become less or more sensitive to the gas core eccentricities.

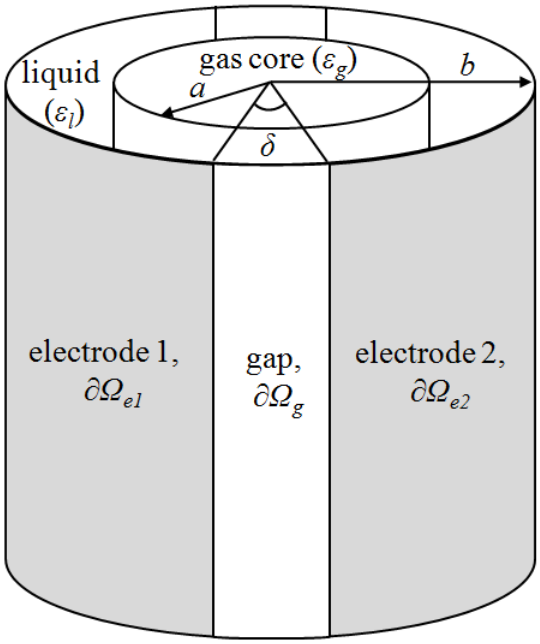

(a) Plate-type sensor

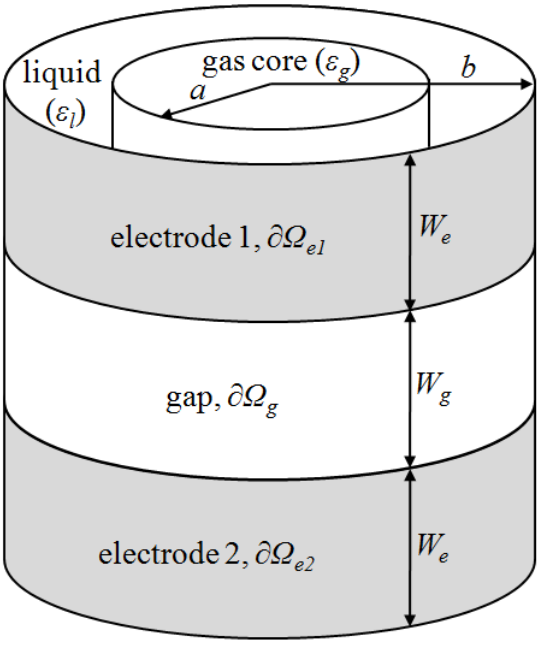

(b) Ring-type sensor

Figure 3.1. Schematic diagrams of an ideal annular flow in two different sensor types.

For numerical analyses, the capacitance for concentric annular flows with various void fractions is first calculated with respect to several sensor gap sizes and the relationship between the dimensionless capacitance and the void fraction is documented for references. Then, the capacitance responses for annular flows with various eccentricities and void fractions are evaluated. Finally, the void fractions for these eccentric annular cases are estimated by comparing their calculated capacitances with the prepared references.

(1) Establishment of a look-up table on the relationship between the dimensionless capacitance C_{con}^{*} and the void fraction α for concentric annular flows for various δ and W_g / b values,

(2) Calculation of the capacitance C_{ecc}^{*} for various eccentric annular flows for the same scenarios as above step,

(3) Evaluation of the void fraction for the eccentric cases α' by comparing C_{ecc}^{*} with the prepared references.

For numerical simulations COMSOL Multiphysics (2008), a commercial software based on the finite element method for the partial differential equations, was used. In numerical calculations three-dimensional geometric arrangements were considered for each sensor type as shown in Fig. 3.1. The applied voltage difference through the electrode pair was set to 1 V. To describe the sensor gap, the zero charge condition, which is analogous to the electrical insulation condition of the conductance method, was applied. The interfacial boundary was assumed to be continuous. Due to the symmetrical feature of the problem, in this work three eccentric annular flows were considered. In the first case the circular gas core

is located in front of the center of the sensor, and for the second and the third cases the gas cores are shifted from the first case by $\theta_{cir} = 45°$ and $\theta_{cir} = 90°$, respectively. These are illustrated by the solid, dashed, and dotted lines in Fig. 3.2, respectively. Also, in all cases the circular annular flows with the void fractions ranging from 0.7 to 0.9 ($\alpha = 0.7 \sim 0.9$) and various eccentricities ($d/b = 0.01 \sim 0.16$, here, d is the closest distance between the gas core and electrode boundaries) were taken into account since the void fraction in annular flow is generally above 0.8 (Todreas and Kazimi 1990). In the plate-type sensor the dimensionless capacitance for the gap angles in the range of 0.05 ~ 1.85 rad were evaluated ($\delta = 0.05 \sim 1.85$ rad), while in the case of the ring-type sensor the gap width-to-radius ratios ranging from 0.1 to 1.0 ($W_g / b = 0.1 \sim 1.0$) were considered.

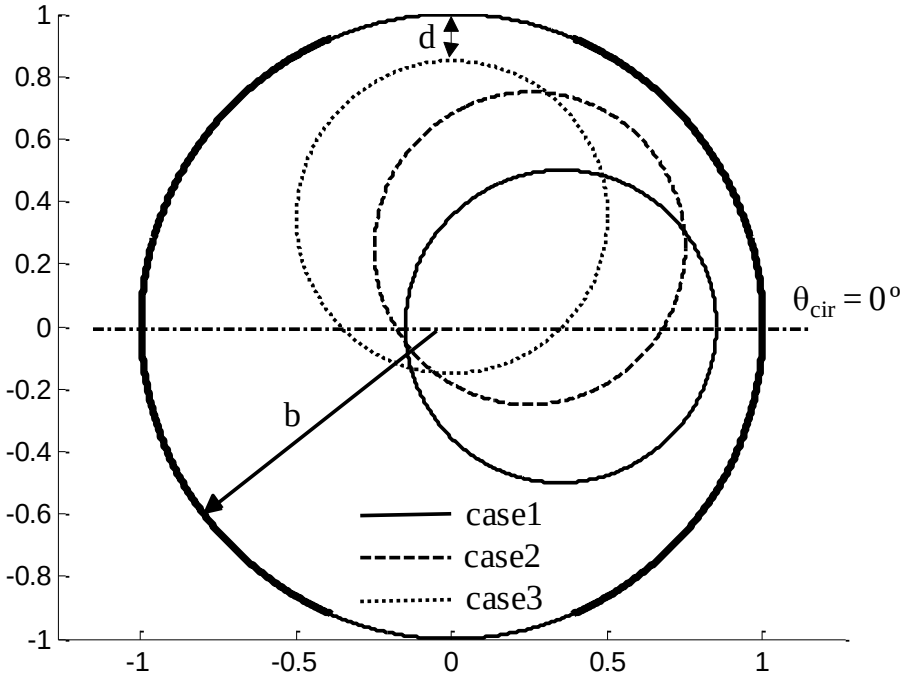

Figure 3.2. Three different cases for numerical simulations.

3.2. Numerical results and discussion

Figure 3.3 shows the relative error between α and α' defined as Eq. (3.9) for various sensor gap sizes.

$$Err = \sqrt{\frac{\sum(\alpha - \alpha')^2}{\sum \alpha^2}}. \tag{3.9}$$

In the plate-type sensors (Fig. 3.3(a)), the relative error decreases with an increase in the sensor gap size and starts increasing at about $\delta = 1.2$ rad. When the sensor gap size is smaller, the electric field is severely distorted, in particular, near the gaps. Similarly, with a larger gap size the edge effect exaggerates the electric field distribution. According to the numerical results, for the plate-type sensor a gap angle equal to about 1 rad ($\delta = 1$ rad) gives a lower relative error than other configurations, indicating that this gap size is less sensitive to the gas core locations.

Figures 3.4 and 3.5 show the cross-sectional views of the electric field distribution for two different plate-type sensors with $\delta = 0.1$ and 1.0 rad, respectively. In these simulations both concentric and eccentric annular flows with $\alpha = 0.7$ were considered, and for the eccentric cases the eccentricity was set to $d/b = 0.06$.

In the case of the smaller sensor gap angle ($\delta = 0.1$ rad) illustrated in Fig. 3.4, the potential gradient is much steeper near the gap than other regions and consequently the non-uniformity of the electric field becomes serious. Contrastively, as the sensor gap angle increases (Fig. 3.5), this trend is significantly mitigated and the electric field distribution becomes much more uniform even for the gas core in front of the sensor gaps (Fig. 3.5(b)). These different characteristics of the electric fields directly affect the capacitance due to the physical relation between the electric field and charge.

For the ring-type sensor, a larger sensor gap size gives a better performance than others (Fig. 3.3(b)). This can be interpreted in the same manner as the plate-type sensor cases. That is, when the sensor gap size is smaller, the electric field is concentrated near the edge and the capacitance responses are heavily distorted. However, as the sensor gap increases this tendency of the electric field to be concentrated near the gap for the smaller gap size is considerably mitigated and the capacitance responses become less sensitive to the locations of the gas core.

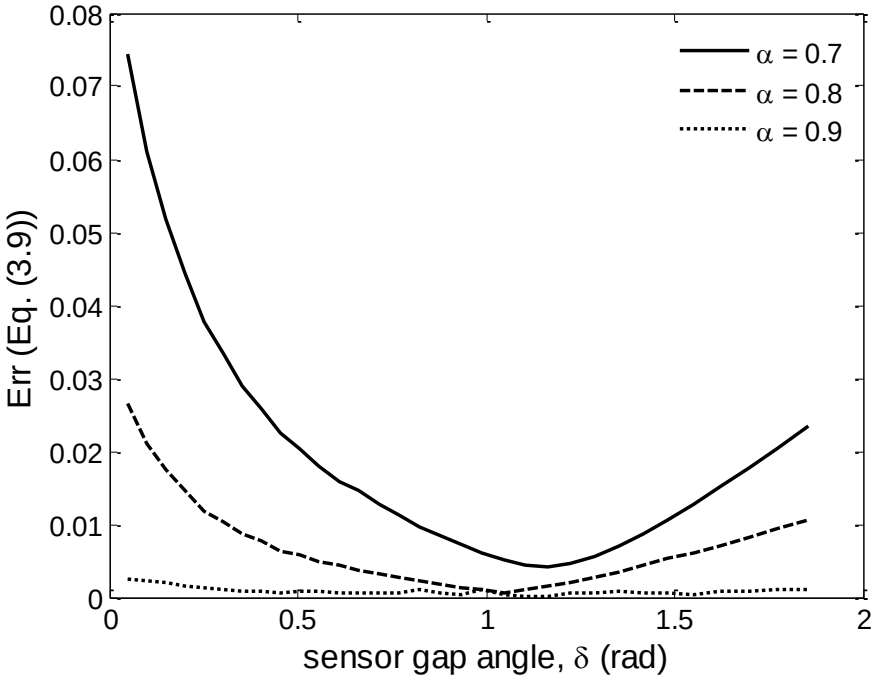

(a) Plate-type sensor

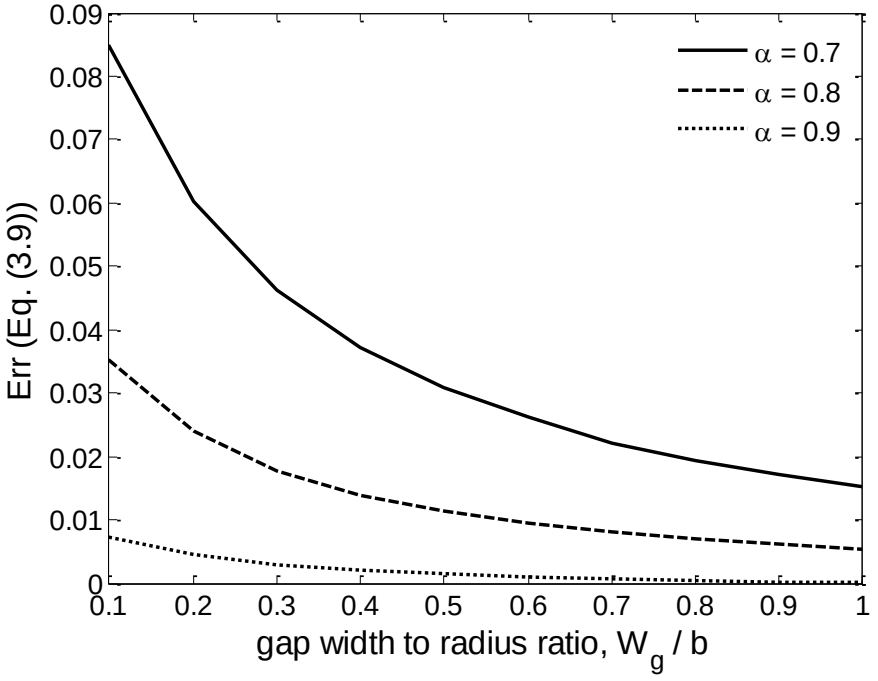

(b) Ring-type sensor

Figure 3.3. Relative errors between α and α' for various sensor gap sizes.

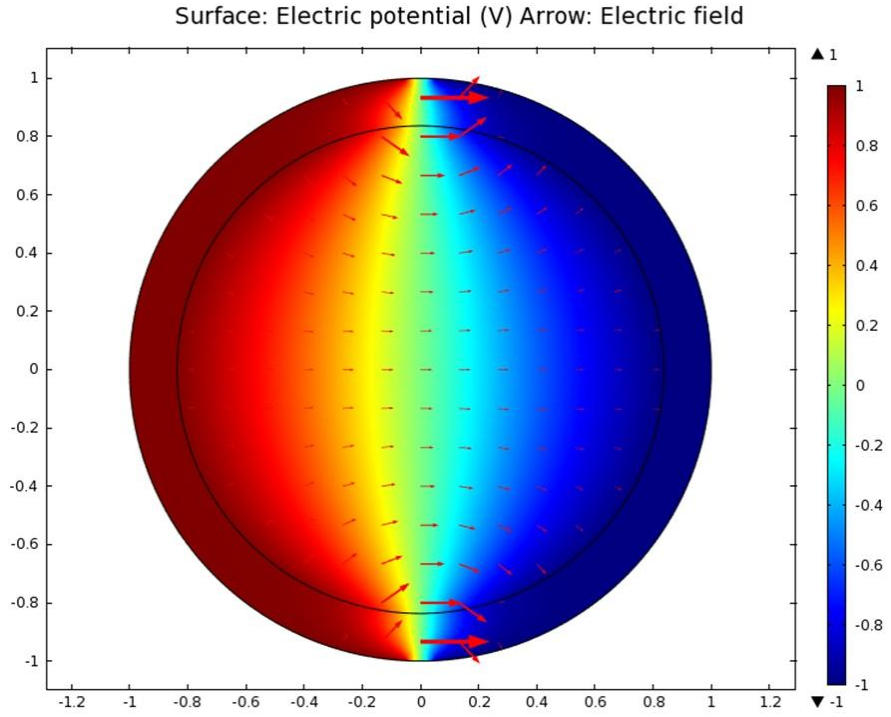

(a) Concentric case with $\alpha = 0.7$

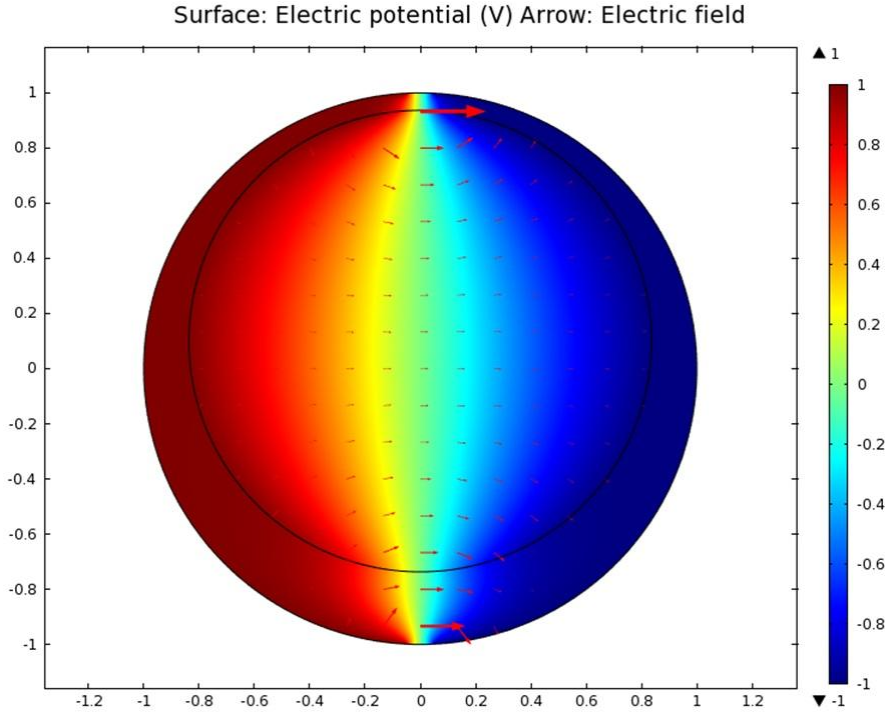

(b) Eccentric case for $\alpha = 0.7$ and $d/b = 0.06$

Figure 3.4. Potential and electric field distribution for the plate-type sensor with δ = 0.1 rad.

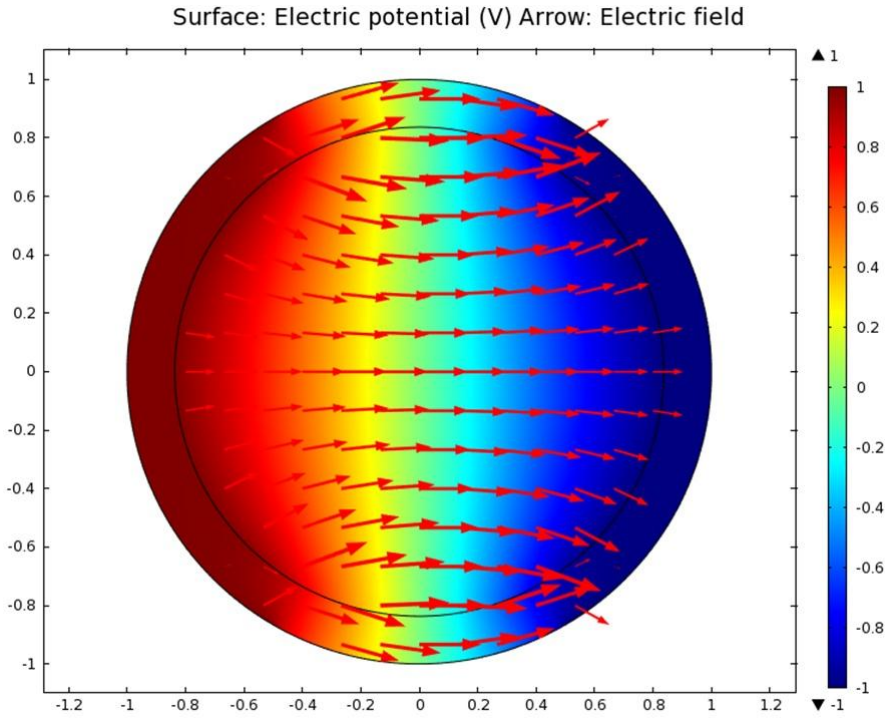

(a) Concentric case with $\alpha = 0.7$

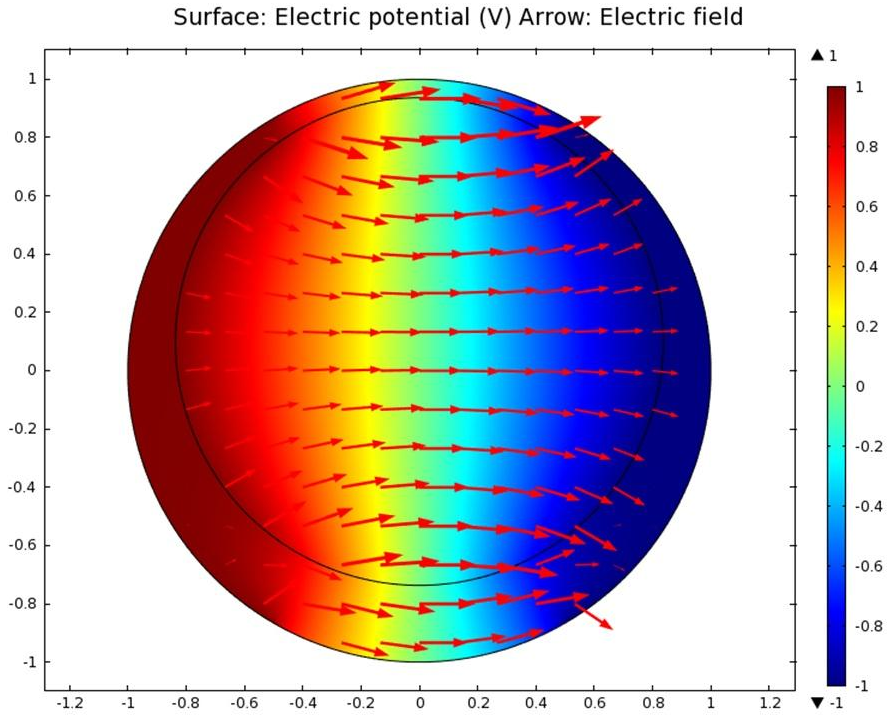

(b) Eccentric case for $\alpha = 0.7$ and $d/b = 0.06$

Figure 3.5. Potential and electric field distribution for the plate-type sensor with δ = 1.0 rad.

3.3. Experiments

To verify the numerical trends, several experiments were conducted. Four cylindrical acryl pipes with 40 mm inner radius were employed for the experiments. Two stainless steel electrodes were flush mounted on the inner wall of the acryl pipes. For both sensor types two different sensor gap sizes were designed for comparison as shown in Fig. 3.6. In the case of the plate-type sensors, one has an electrode pair which is separated by 2 mm ($\delta = 0.05$ rad), while two electrodes of the other sensor are separated by 42 mm ($\delta = 1.04$ rad). Similarly, for the ring-type sensors the first and the second ones are separated by 4 and 40 mm gaps that is, $W_g / b = 0.1$ and $W_g / b = 1.0$, respectively. Table 1 summarizes the specifications of each sensor configuration.

The reference capacitances, C_g and C_ℓ, were measured by filling the sensors with an acryl rod with 40 mm radius and water only, respectively. To describe the void fractions, three acryl rods corresponding to the void fractions 0.7, 0.8, and 0.9 were fabricated as shown in Fig. 3.7. The capacitances were measured with an Agilent 4284A LCR meter whose basic accuracy is 0.05 % for the full scale. The applied frequency and voltage were set to 1 MHz and 1 V, respectively, and this sinusoidal AC voltage were provided to an Agilent 16089B Kelvin Clip Leads connected with the LCR meter.

For air-water two-phase flows under the standard temperature and pressure, the electrical conductivity and permittivity of water are generally 0.005 S/m and 7 × 10^{-7} F/m ($\sigma_\ell = 0.005$ S/m and $\varepsilon_\ell = 7\times10^{-7}$ F/m). In this adiabatic condition, a theoretical estimation gives $\sigma_\ell \sim \omega\varepsilon_\ell$ for $f = 1$ MHz, implying that the resistance is much more dominant below this frequency, but the role of the reactance becomes more important in the impedance over 1

MHz. Due to this reason, most researches related to the conductance method have adopted relatively low signal frequencies between 10 and 100 kHz (Andreussi *et al.* 1988, Tsochatzidis *et al.* 1992, Fossa 1998, Song *et al.* 1998, Devia and Fossa 2003), while those associated with the capacitance method have made measurements at a frequency over 1 MHz (Abouelwafa and Kendall 1980, Shu *et al.* 1982, Lowe and Rezkallah 1999, Jaworek *et al.* 2004, Canière *et al.* 2008, Strazza *et al.* 2011). A further discussion on the signal frequency is again presented in Chapter 4.

At each location 100 measurements were repeated for each given void fraction and sensor design. The measured capacitances were approximately in the range of 7.0 to 126.0 pF for sensor A and 1.3 to 60.0 pF for sensor B of the plate-type sensors. In the case of the ring-type sensors, the measured capacitance ranges were roughly from 13.0 to 171.0 pF for sensor C and from 2.6 to 58.0 pF for sensor D, respectively (Fig. 3.6). The standard deviations of the measured capacitances were within 0.1% for all sensors.

According to Fig. 3.8, for the plate-type sensor with $\delta = 0.05$ rad (sensor A), the dimensionless capacitances for the concentric case significantly deviated from those for the eccentric cases; in particular, when the acryl rod is located near the gap the deviation is worse than other locations as expected from the numerical study. However, for the optimized plate-type sensor with $\delta = 1.04$ rad (sensor B), all capacitance signals for the eccentric cases well match those for the concentric cases irrespective of the locations of the acryl rods. Similarly, the optimized ring type sensor with $W_g / b = 1.0$ (sensor D) shows much better performance than the non-optimized one (sensor C). The optimized sensors, of course, show the better linearity to void fraction changes (Figs. 3.8 and 3.9(b)).

Table 3.1. Specifications of capacitance sensors.

	Plate-type		Ring-type	
	Sensor A	Sensor B	Sensor C	Sensor D
Radius of sensor (mm)	40	40	40	40
Width of sensor (mm)	40	40	20	20
Gap angle (rad)	$\delta = 0.05$	$\delta = 1.04$		
Gap width-to-radius			$W_g / b = 0.1$	$W_g / b = 1.0$

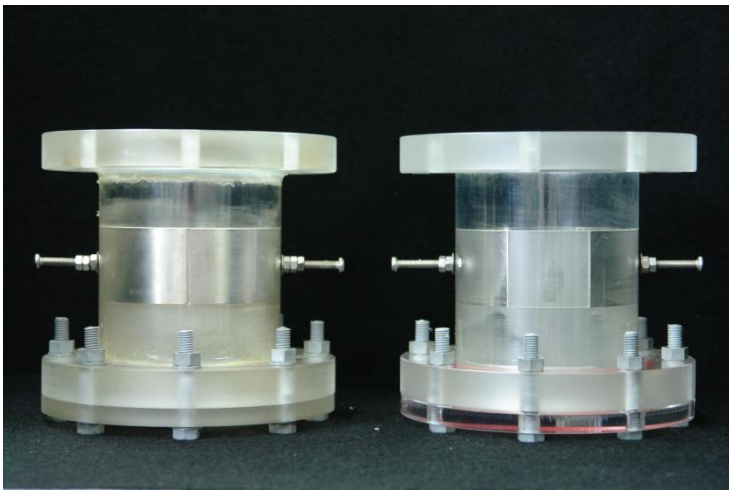

(a) Plate-type sensors: the left and right ones are denoted sensors A and B

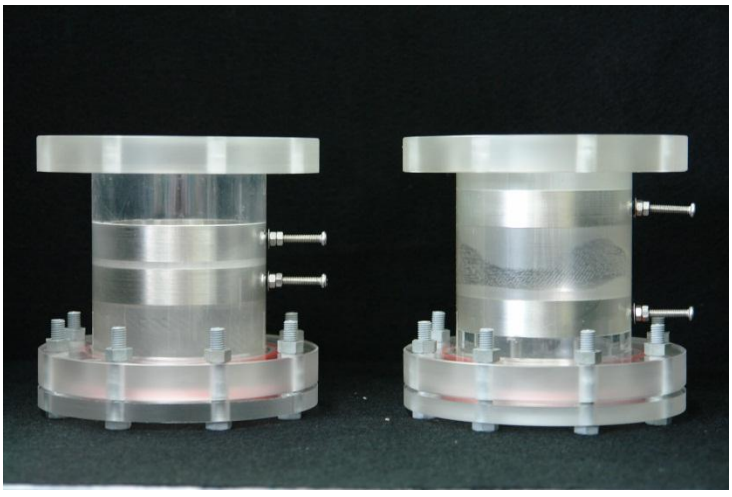

(b) Ring-type sensors: the left and right ones are denoted sensors C and D

Figure 3.6. Capacitance sensors with different sensor gap sizes.

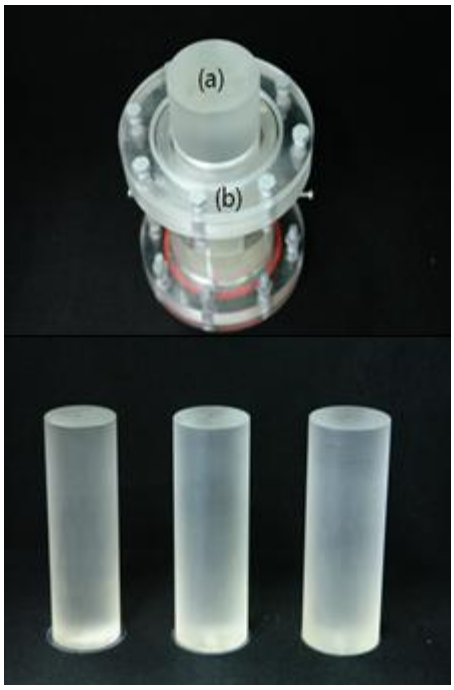

Figure 3.7. Acryl rods for void fractions. (a) acryl rod, (b) flange.

From Fig. 3.10, it can be seen that when the proposed plate-type sensor with $\delta = 1.04$ rad is used the void fraction in the annular flows can be measured within 2.5% relative error, while the non-optimized one gives maximum 8.0 % relative error. Similarly, for the ring-type sensors the optimized one gives 1.5 % relative error, which is three to four times better than the non-optimized one (about 5.5% relative error). Also, the experimental evidences indicate that the optimized ring-type sensor shows even better performance than the plate-type sensors on the whole. However, considering the fact that the measurement volume should be as small as possible for local measurement the plate-type configuration may be more practical (see sensors B and D).

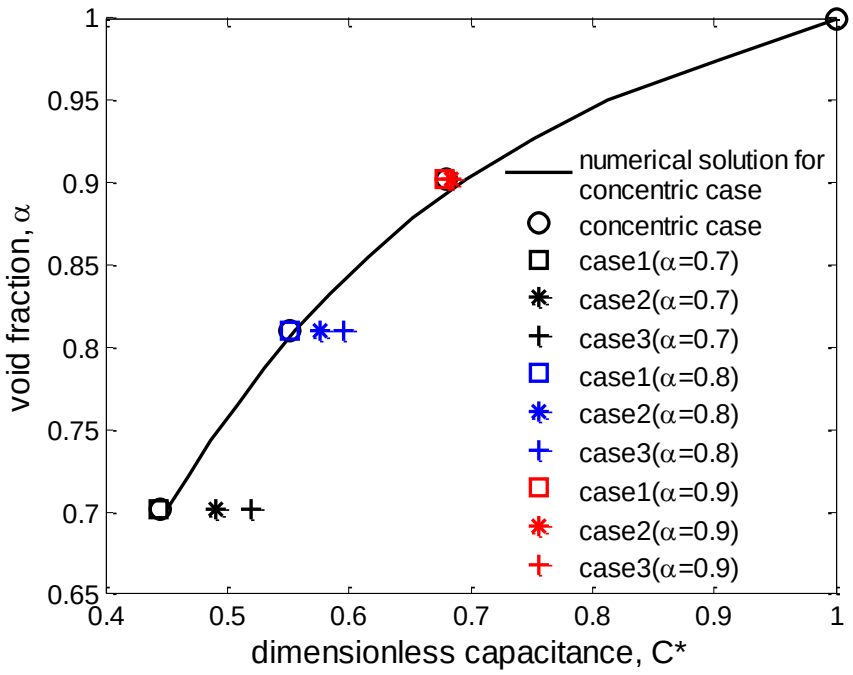

(a) Sensor A ($\delta = 0.05$ rad)

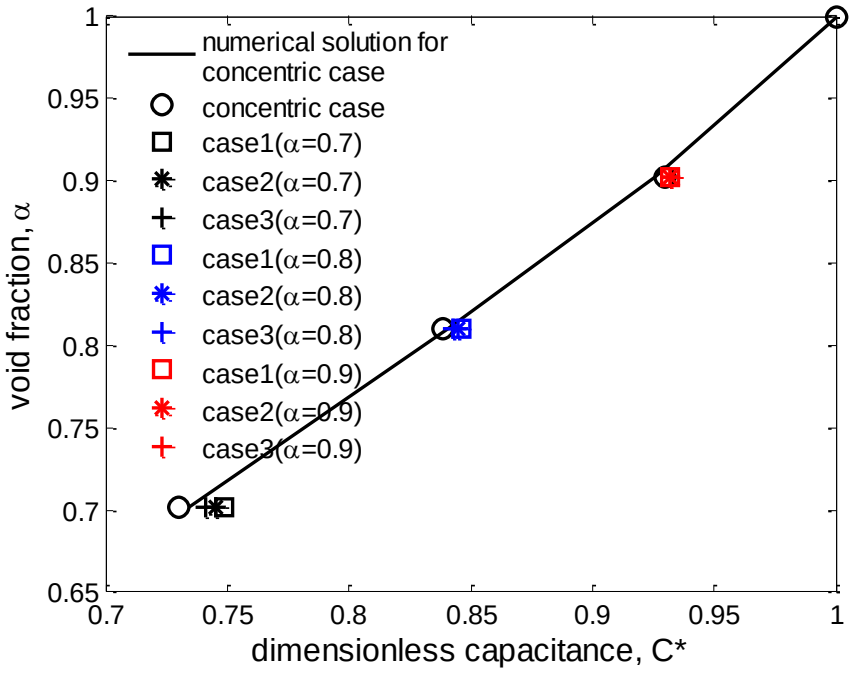

(b) Sensor B ($\delta = 1.04$ rad)

Figure 3.8. Comparison between numerical and experimental results for two different plate-type sensors.

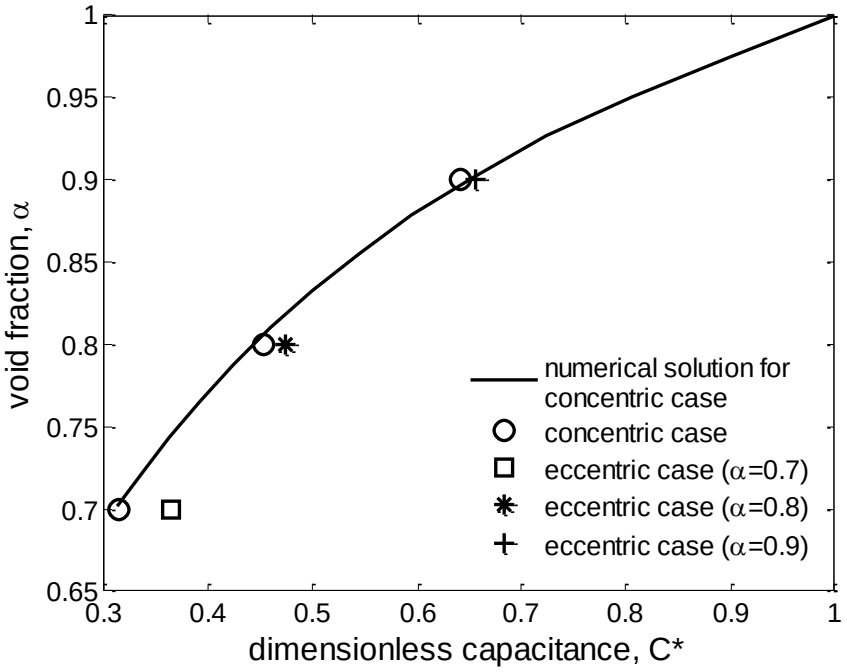

(a) Sensor C ($W_g / b = 0.1$)

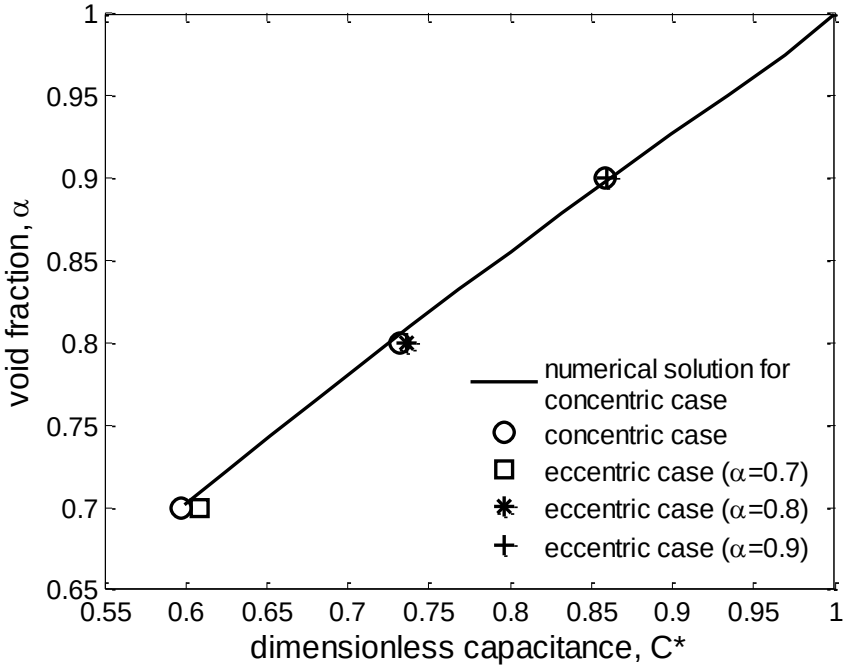

(b) Sensor D ($W_g / b = 1.0$)

Figure 3.9. Comparison between numerical and experimental results for two different ring-type sensors.

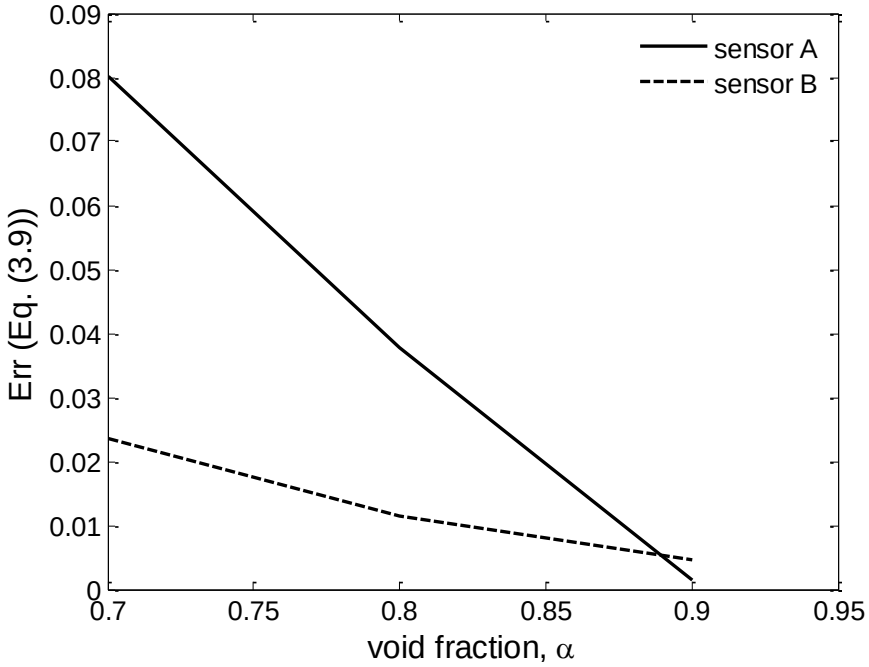

(a) Plate-type sensors.

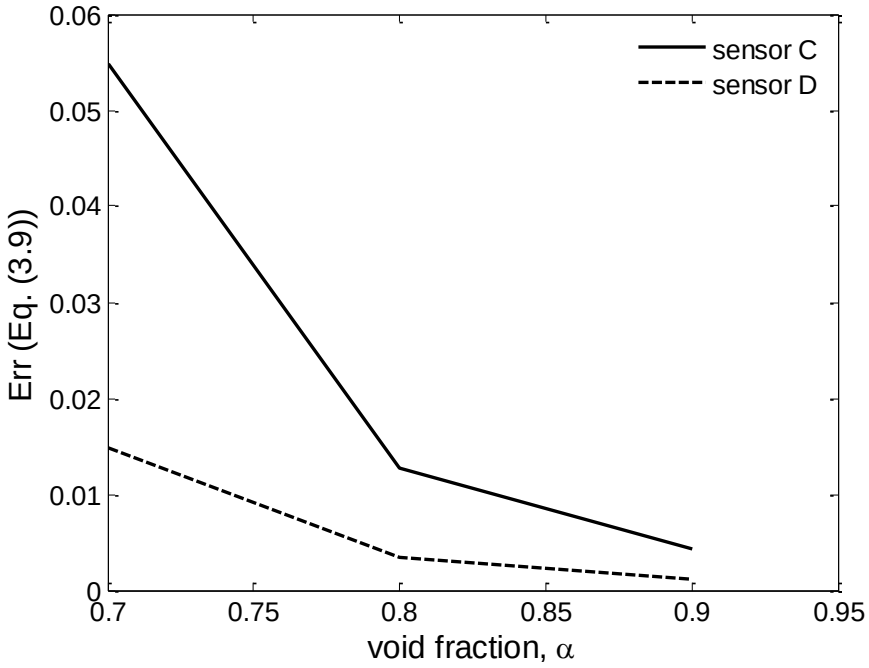

(b) Ring-type sensors

Figure 3.10. Comparison for performance of void fraction measurement.

3.4. Summary

The effect of gas core fluctuations in annular flows on capacitance responses may be an important factor to be considered for the sensor design. This chapter performed the numerical analyses and the experiments to find the optimal configuration providing reliable void fraction measurement irrespective of the gas core fluctuations. The main conclusions are summarized as follows.

- For the plate-type sensors with smaller gap sizes, the electric field distribution was not uniform across the sensor and consequently the capacitance was significantly affected. In particular, when the gas core is located near the gap the situation was the most serious. Similarly, in the case of higher gap sizes ($\delta > 1.2$ rad) the electric field was considerably exaggerated due to the edge effect. Similar observation was also made in the ring-type sensors.
- The numerical study indicated that when a particular size of the sensor gap ($\delta = 1.0$ rad) was used the capacitance response of the plate-type sensor showed the better performance in view of the sensitivity for the gas core fluctuations. For the ring-type sensors the larger gap size gave the better characteristic than others. These findings were also verified from the comparison experiments.
- It is expected that the optimal configurations obtained in this work may be even valid for the conductance method due to the physical similarity between the conductance and capacitance method.

4. An electrical impedance sensor for liquid level measurements of air-water two-phase stratified flows in horizontal pipes

4.1. Problem description and numerical modeling

Consider a liquid-gas two-phase stratified flow through a ring-type sensor as illustrated in Fig. 4.1. As discussed in Section 2.1, the potential distribution for each phase can be determined by the following Laplace equations:

$$\nabla \cdot \left(\sigma_\ell + i\omega\varepsilon_\ell \right) \nabla \phi_\ell = 0 \quad \text{for liquid phase,} \tag{4.1}$$

$$\nabla \cdot \left(\sigma_g + i\omega\varepsilon_g \right) \nabla \phi_g = 0 \quad \text{for gas phase,} \tag{4.2}$$

where σ_ℓ and σ_g are the electrical conductivity for the liquid and gas phases, and ε_ℓ and ε_g represent the permittivity for them, respectively. In above two equations, i is the imaginary unit and ω is the angular frequency corresponding to $2\pi f$ where f is the applied frequency. Also, ϕ_ℓ and ϕ_g are the potential distribution to be determined for each phase. For a given applied voltage difference through two ring electrodes, the electrical impedance can be evaluated from Ohm's law that is, $Z = \Delta V / I = R + iX$. Writing the electrical impedance in terms of the magnitude we get $|Z| = \sqrt{R^2 + X^2}$. Here, R and X are the electrical resistance and reactance evaluated from the relation between the applied voltage difference and the current density obtained from the solution to the Laplace equations (4.1) and (4.2) (see Section 2.2). For convenience, now let us define the dimensionless impedance as follows:

$$|Z^*| = \frac{|Z_\ell|}{|Z|}. \tag{4.3}$$

Here, $|Z_\ell|$ is the norm of the electrical impedance for the sensor filled with the liquid phase only and $|Z|$ is the impedance magnitude for an arbitrary liquid level defined as

$$h^* = \frac{h}{D}, \tag{4.4}$$

where h and D represent the liquid level and the pipe diameter, respectively (Fig. 4.1). Therefore, the definition of the dimensionless impedance indicates that maximum $|Z^*| = 1$ at $h^* = 1$ and minimum $|Z^*| = 0$ at $h^* = 0$.

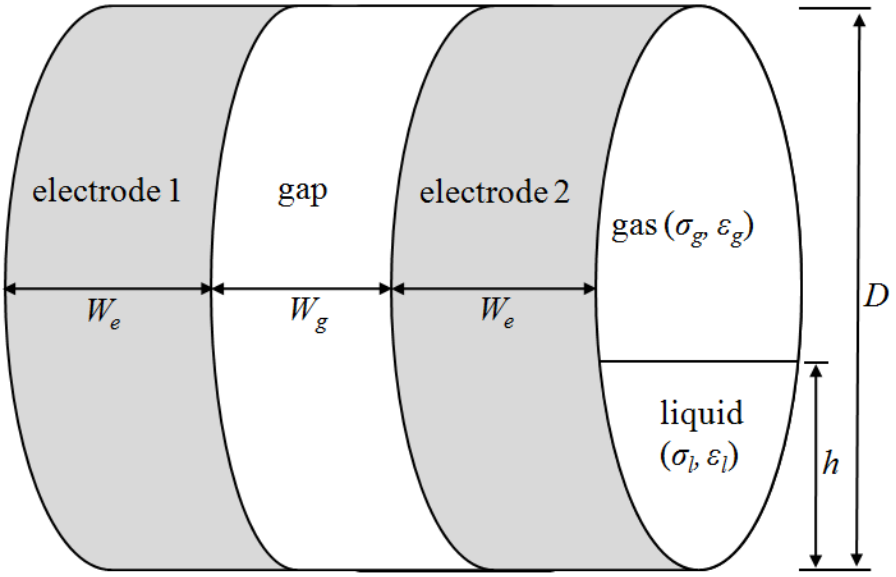

Figure 4.1. A stratified flow in a ring-type impedance sensor.

In numerical simulations, the magnitude of the applied voltage difference was set to 1 V, and the signal frequencies from 1 kHz to 1 MHz were tested. The gap between the electrodes was electrically insulated and the interface between the liquid and gas phases was assumed to be continuous in the potential and the current density. On the upstream and the downstream surfaces, a homogeneous Neumann condition was used. Considering air-water two phase flows the electrical properties of each phase were set to $\sigma_\ell = 0.005$ Sm^{-1}, $\sigma_g = 0$ Sm^{-1}, $\varepsilon_\ell = 80\varepsilon_0$ and $\varepsilon_g = \varepsilon_0$, where ε_0 is the permittivity for vacuum. Also, the electrode width-to-diameter ratios ranging from 0.1 to 0.3 by 0.05, and the gap-to-diameter ratios from 0.1 to 1.0 by 0.1 were considered for numerical calculations ($W_e / D = 0.1 \sim 0.3$ and $W_g / D = 0.1 \sim 1.0$).

4.2. Numerical results and verification

To find the optimal size of the electrode and the gap, which generates linear responses to water level variations, the following relative error was introduced:

$$Err = \frac{1}{N}\sum_{n=1}^{N}\frac{\left|\left|Z^*_{linear}\right| - \left|Z^*_n\right|\right|}{\left|Z^*_{linear}\right|}, \tag{4.5}$$

where $\left|Z^*_{linear}\right|$ is the ideal linear impedance response ($\left|Z^*_{linear}\right| = h^*$) and $\left|Z^*_n\right|$ denotes the impedance signal for arbitrary W_e / D and W_g / D values and h^*. The subscript n represents the *n*th dimensionless water level considered in the numerical simulations. In this work $N = 11$ dimensionless water levels were taken into account, in which each water level corresponds to the liquid volume fraction from 0 to 1 by 0.1.

Figure 4.2 shows the numerical results for the electrical impedance responses to the

water level changes with respect to various geometrical ratios and frequencies. The overall trends on the relative error for each configuration are almost identical at each frequency. That is, the effect of the frequencies on the sensor linearity is marginal. On the other hand, the effect of W_e / D and W_g / D on the relative error are significant. Among all cases considered the configuration with $W_e / D = 0.3$ and $W_g / D = 0.2$ gives the minimum relative error from the linear responses. However, considering that the length of the sensor should be as short as possible for local measurement the ring-type sensor with $W_e / D = 0.25$ and $W_g / D = 0.2$, which shows a comparable error, may be more favorable.

To verify the numerical results, a ring-type sensor with 40 mm diameter was designed as shown in Fig. 4.3. The widths of two ring electrodes are 10 mm ($W_e / D = 0.25$), and the gap width is 8 mm ($W_g / D = 0.2$). The electrodes, made from the stainless steel 2 mm thick, are flush mounted on the inner surface of a teflon spool.

Static experiments for stratified flows were performed with the ring-type sensor laying horizontally, into which specified amounts of water are injected. For electrical impedance measurement, a Hioki IM 3570 Impedance analyzer (0.08% basic accuracy for 1 V $\leq V_{app} \leq$ 5 V at room temperature) with an L2000 4-terminal probe was adopted. The ring-type sensor was connected with the L2000 4-terminal probe. 1 V of 1 MHz sinusoidal AC voltage was applied to a ring electrode through the clip lead while the other is kept at ground. For each water level, 100 electrical impedance measurements were repeated.

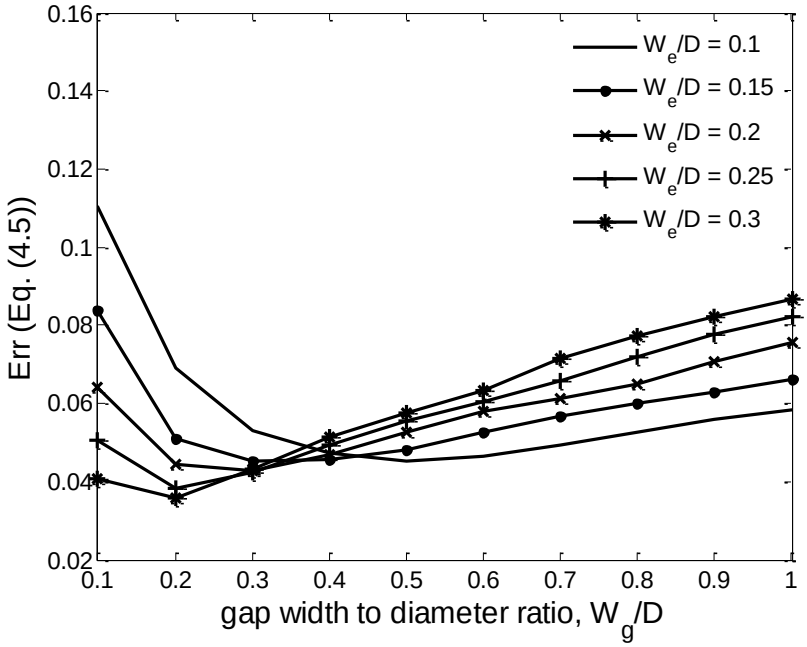

(a) 1 kHz

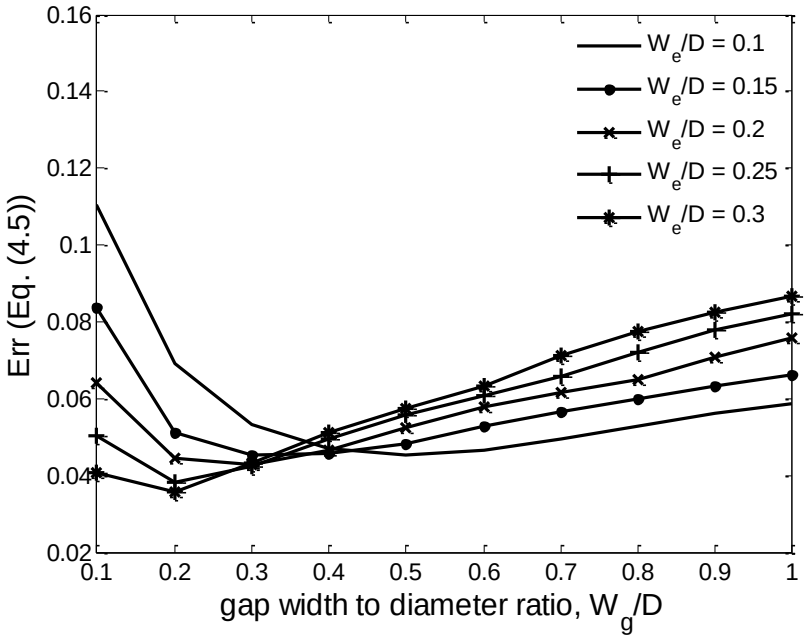

(b) 10 kHz

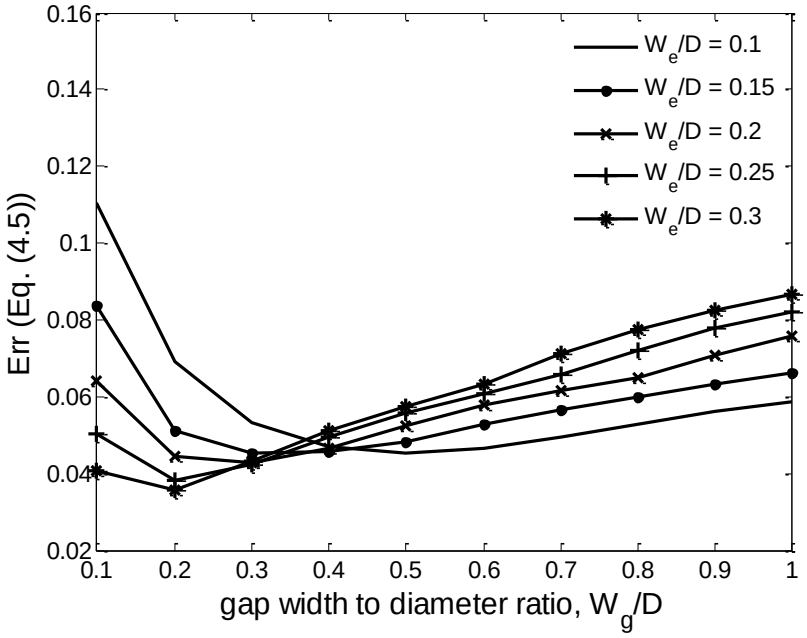

(c) 100 kHz

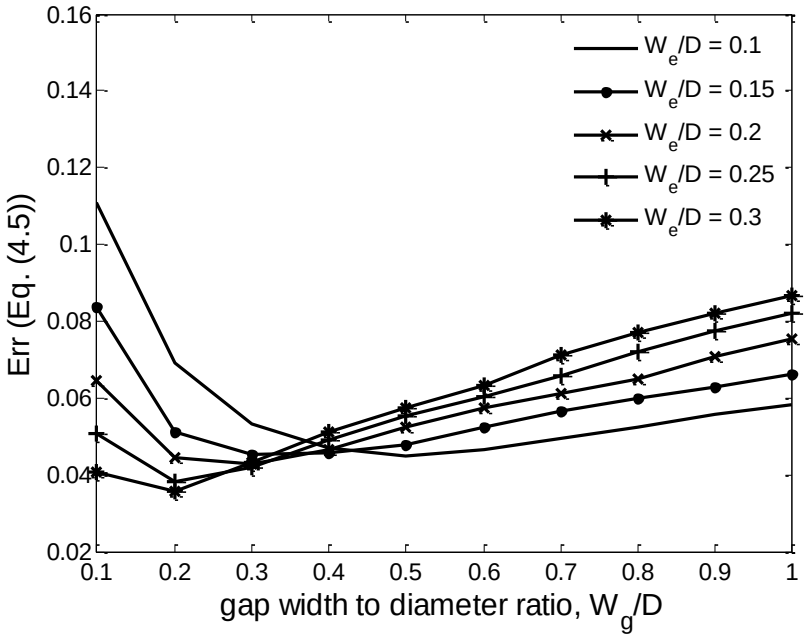

(d) 1 MHz

Figure 4.2. Relative errors between ideal linear and calculated impedance values for various W_e / D, W_g / D values and frequencies.

Figure 4.4 shows the comparison of the numerical and experimental results with the ideal linear response for the impedance, resistance and reactance. On the whole, the experimental evidences show very good agreements with theoretical predictions, also a good linear relationship between the dimensionless impedance (resistance/reactance) and the water level is confirmed when the proposed sensor dimensions are used for water level measurement.

In all cases, the maximum deviation from the ideal linear response is 0.023 (0.93 mm) for the impedance in terms of h^* (h for $D = 40$ mm). Similarly, those for the resistance and reactance cases are 0.036 (1.44 mm) and 0.029 (1.16 mm), respectively. Their contributions to the impedance are $|R|^2 / |Z|^2 = 76.2\%$ and $|X|^2 / |Z|^2 = 23.8\%$ for $h^* = 0.5$, which are comparable orders to the theoretical estimation by $\sigma_\ell / \omega\varepsilon_\ell$.

The maximum uncertainty of the impedance measurements is $U_{\max,Z} = \sqrt{Z_{B,\max}^2 + Z_{P,\max}^2} = 10.6\ \Omega$ with 95% confidence level, where $Z_{B,\max}$ and $Z_{P,\max}$ are the bias and precision limits. Similarly, the maximum uncertainties in terms of the dimensionless impedance and corresponding water level are $U_{\max,Z^*} = 0.0015$ and $U_{\max,h^*} = 0.0013$, respectively.

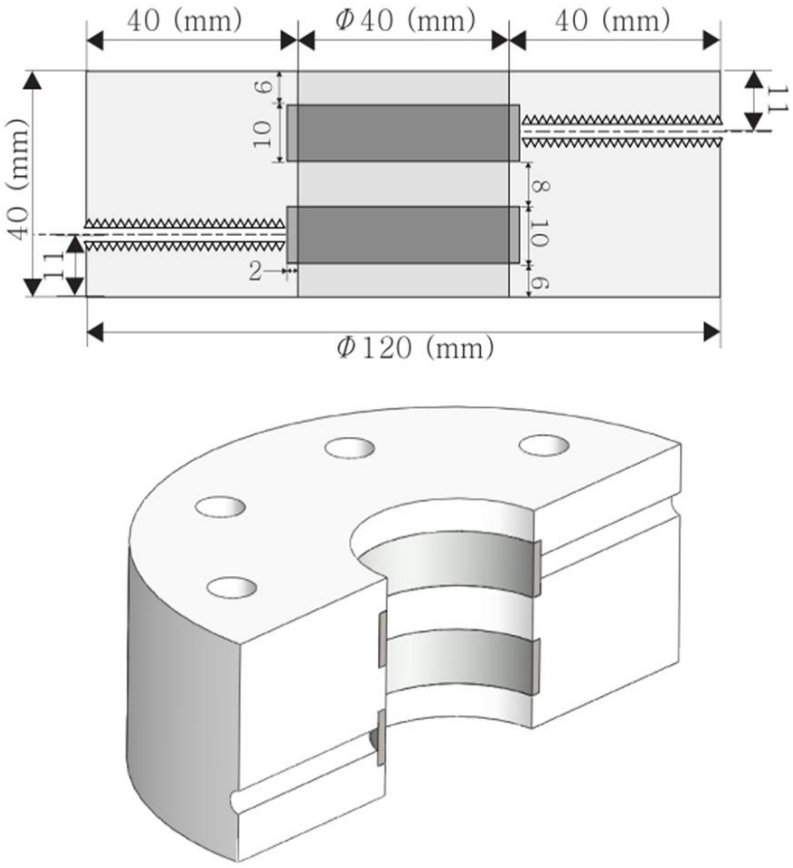

(a) Schematic of the designed sensor

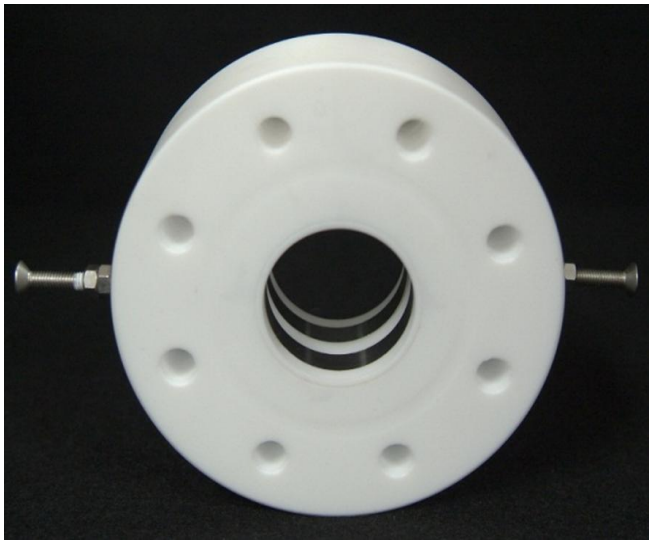

(b) Photograph of the designed sensor

Figure 4.3. A schematic and a photograph of the proposed impedance sensor.

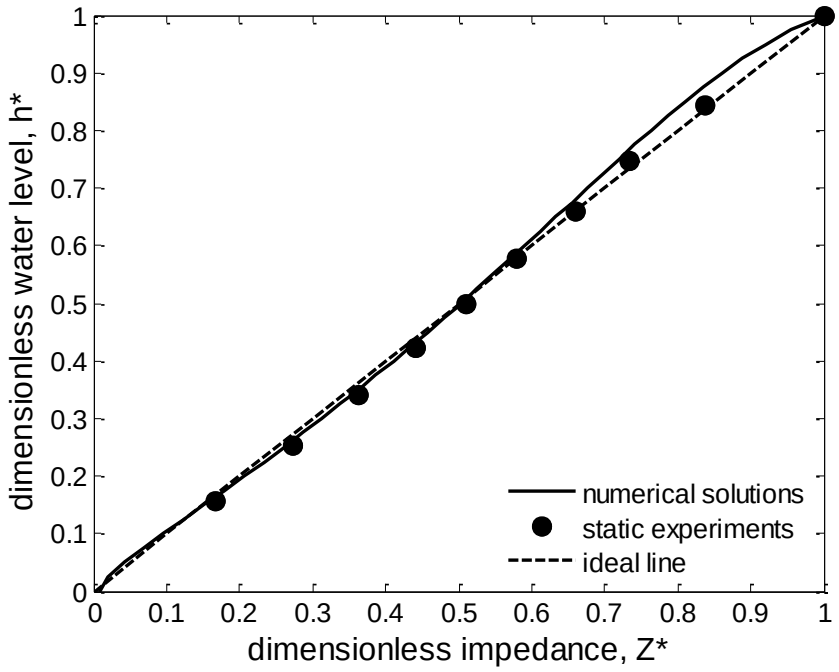

(a) Impedance

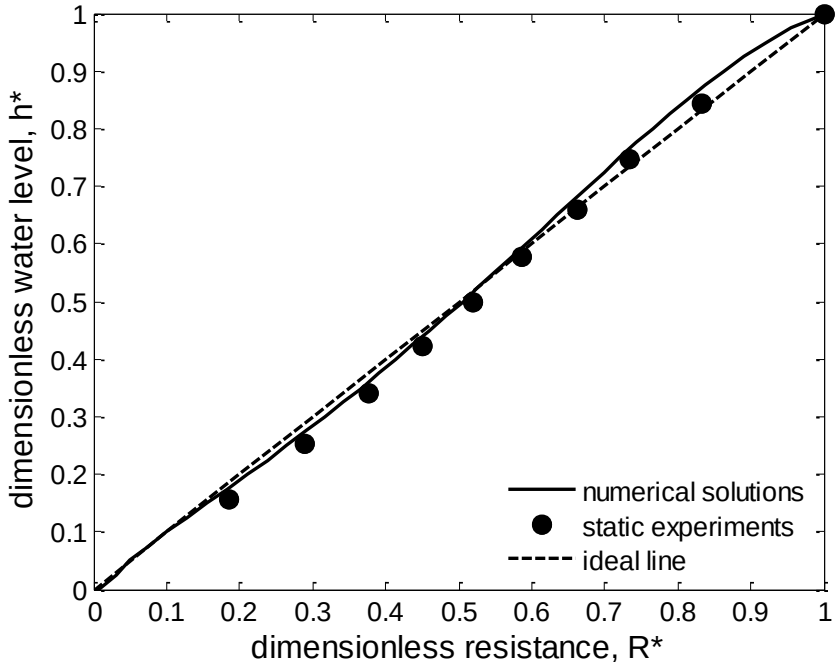

(b) Resistance

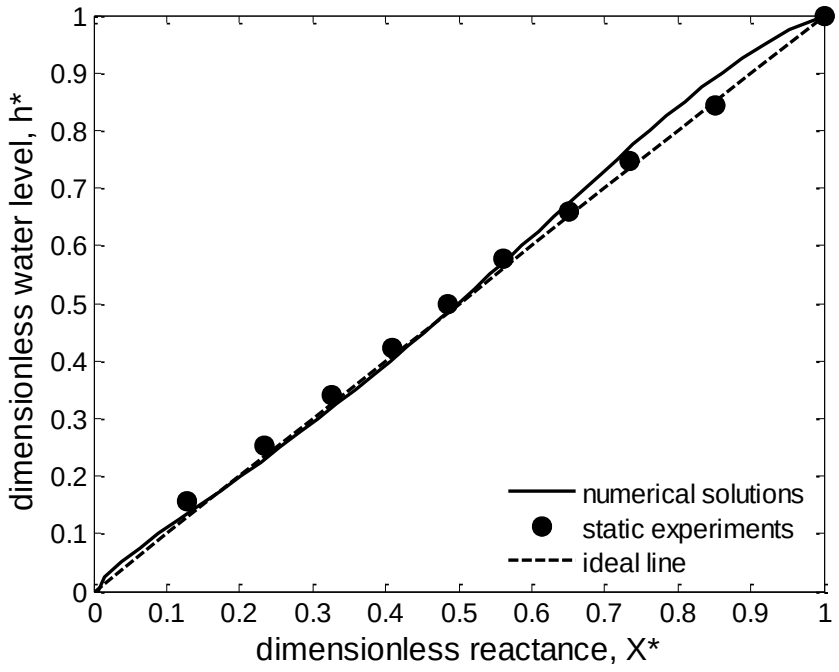

(c) Reactance

Figure 4.4. Comparison of numerical solutions and static experiments with the linear response at 1 MHz.

4.3. Experimental setup for dynamic experiments

4.3.1. Horizontal loop

Figure 4.5 shows a schematic of a horizontal experimental loop. As illustrated in this figure, water in a main collection tank (1) is lifted by a 5 HP pump (2), and then this pumped water flows through a pre-heater to control the operating fluid temperature (3, 4) and a Coriolis water flow meter (5). Finally, water enters an entrance. Similarly, air compressed by a 15 HP compressor (10) flows into an air dryer for the removal of water contents in the compressed air (11), and then it flows into the entrance via a Coriolis air flow meter (12). These two fluids are at last combined in a mixer, and then flow into an acrylic test section 40

mm in diameter and roughly 5200 mm in length (6). After they flow through the location of a high speed camera set-up (13) and the impedance sensor (14) installed nearby, air is blown away from a separator (7) and the water is collected in an auxiliary tank (8). Water, finally, is lifted by a 3 HP auxiliary pump (9) and then again enters the main collection tank (1). Figure 4.6 provides a photograph for the horizontal test section, and the installation of the high-speed camera and the designed impedance sensor. The specifications of the flow measurement instruments are summarized in Table 4.1.

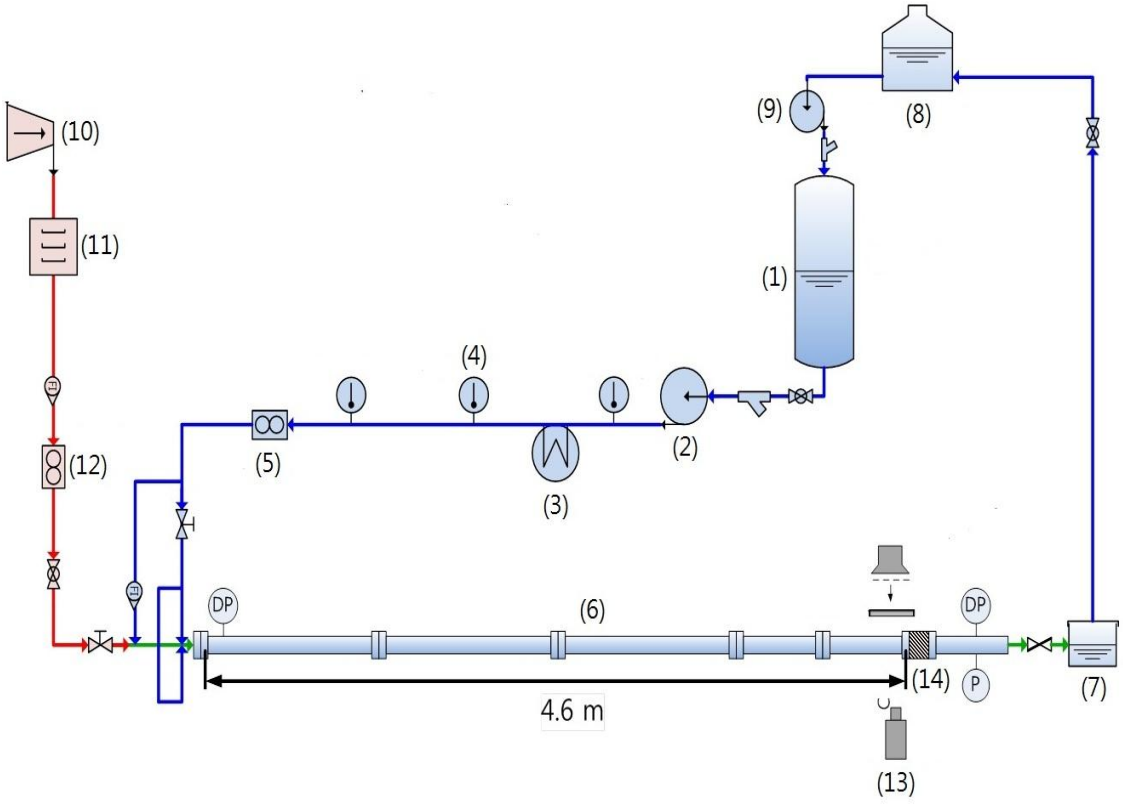

Figure 4.5. A schematic of a horizontal-experimental loop.

Figure 4.6. High-speed camera and impedance sensor installations.
(a) horizontal pipe, (b) high-speed camera, (c) impedance sensor.

Table 4.1. Specifications of flow measurement instruments.

Instrument	Measurement range	Accuracy	Temporal resolution
Water mass flow meter	0 ~ 400 kg/min	±0.15% FS	N/A
Air mass flow meter	0 ~ 15 kg/min	±0.2% FS	N/A
Differential pressure transmitter	- 9.03 ~ 9.03 psi	±1.0% FS	N/A
Pressure transmitter	14.65 ~ 150.84 psi	±1.0% FS	N/A
K-type thermocouple	- 200 ~ 1200 ℃	±1.5 ℃ (Temperature range: 0 ~ 400℃)	N/A
Impedance analyzer	0 ~ 9.9999 Ω	±0.08 % rdg	Up to 2000 fps
High speed camera	N/A	N/A	Up to 3600 fps (full image size)

4.3.2. High-speed camera and image processing

To evaluate the performance of the designed sensor, the high-speed camera, Fastcam SA4, which can monitor two-phase flows at 3600 fps with 1024 × 1024 resolution, was employed with a 1 kW halogen spotlight and a diffuser as briefly illustrated in Figs. 4.5 and 4.6. Also, a scale bar was attached on the inner wall of the pipe for the calibration. For the determination of the water level from visualized images, the Sobel edge detection method was applied (Jung and Lee 2005). In this method, the edge represents the locus where the brightness of the images abruptly changes from high to low side or vice versa. In Fig. 4.7(a), for example, the brightness change near the interface between the air and water phases which is illustrated as part (I) is quite steep; however, the brightness change in the air phase represented by part (II) is negligibly small, implying that no edges may be found in this region. In mathematical description, this concept can be written by evaluating the gradient for the brightness change in two-dimensional space. That is,

$$G(x) = \frac{\partial f(x,y)}{\partial x} = \frac{f(x+dx,y) - f(x,y)}{dx}, \tag{4.6}$$

$$G(y) = \frac{\partial f(x,y)}{\partial x} = \frac{f(x,y+dy) - f(x,y)}{dy}, \tag{4.7}$$

where $G(x)$ and $G(y)$ denote the edges dependent on x and y directions of the images, respectively. The magnitude of the edge for a certain x and y position is given by

$$G = |G(x)| + |G(y)|. \tag{4.8}$$

Figure 4.7(b) shows a processed image by the Sobel edge detection method, and in this figure the edges are denoted by the white lines and their magnitudes are expressed as the definition of the lines. Despite the application of the Sobel edge detection method, the images still

contain so numerous edges near the interface that the determination of the water level may not be straightforward. To resolve this difficulty, these images are reprocessed by extracting the edges with the maximum magnitude $G_{\max}$ (Fig. 4.7(c)).

Now, the water level for a fixed x coordinate can be evaluated by the geometrical relation given as

$$h_j^* = \frac{1}{2}\left[1 - \cos\left(2P_j / D\right)\right]. \tag{4.9}$$

Here, the subscript 'j' denotes the jth edge and P_j is the perimeter wetted by the water for the jth edge. The instantaneous water level is now estimated by averaging h_j^* located in different elevations. That is,

$$\bar{h}_k^* = \frac{1}{N_e}\sum_{j=1}^{N_e} h_j^*, \tag{4.10}$$

where the subscript 'k' is the kth measurement frame and N_e is the number of the extracted edges. Finally, the time-averaged water level can be obtained by averaging the instantaneous water levels over the measurement frames. That is,

$$\tilde{h}^* = \frac{1}{N_t}\sum_{k=1}^{N_t} \bar{h}_k^*, \tag{4.11}$$

where N_t is the total measurement frame.

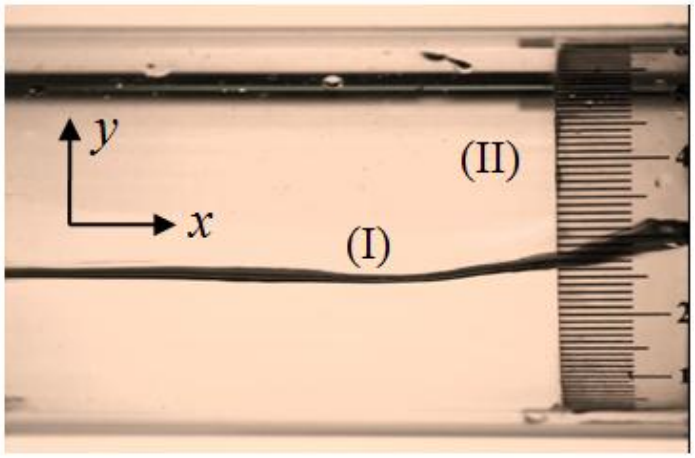

(a) Real image

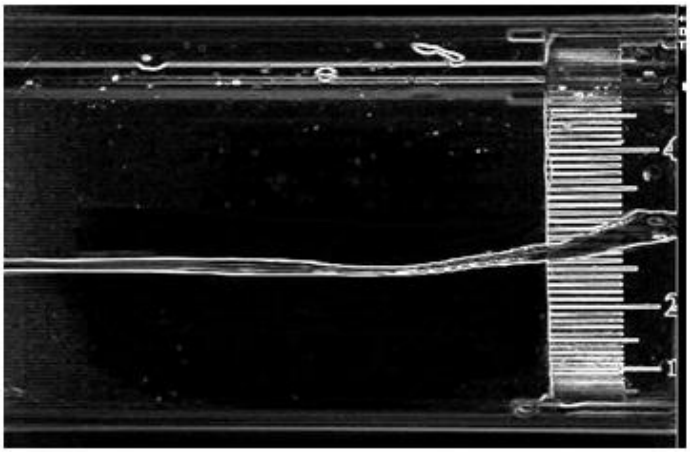

(b) Processed image by the Sobel edge detection method

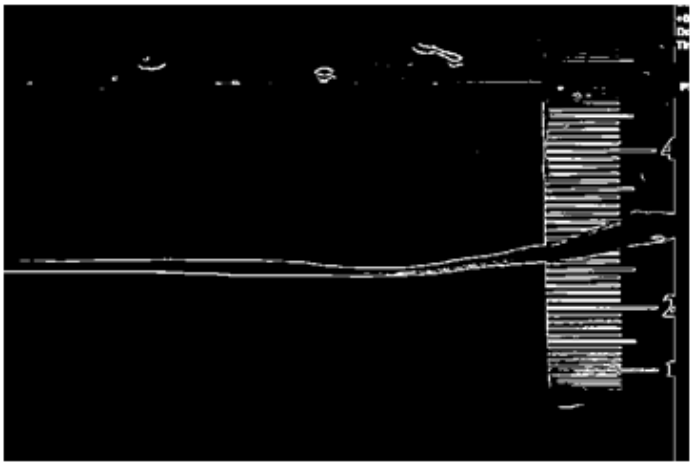

(c) Reprocessed image

Figure 4.7. An example of image processing.

4.4. Experimental results

For loop expriments, the impedance sensor was installed 4600 mm away from the entrance, and simultaneously the high speed camera was set up 50 mm away from it as illustrated by parts (13) and (14) in Figs. 4.5 and 4.6. The superficial velocities ranging from 0.03 to 0.09 m/s for water and from 0 to 8 m/s for air were used (j_ℓ = 0.03~0.09 m/s, j_g = 0 ~ 8 m/s), since higher superficial velocities above these ranges cause the flow regime transition from stratified flows to slug flows, which was also oberved in the experimental flow regime map by Mandhane *et al.* (1974) and in the Taitel and Dukler's semi-theoretical model (1976). For each stratified flow, the instantaneous dimensionless water levels for given time sequences were evaluated by relating the measured impedance signals to the prepared look-up table from the static experiments. Also, two-phase stratified flows were captured by the high-speed camera. These captured images are then processed as demonstrated in the preceding section.

Figure 4.8 shows some examples for the comparison of the instantaneous water level measurements between the proposed sensor and the high-speed camera. When the interface between the air and water phases is smooth as shown in Fig. 4.8(a), the performance of the water level measurements is excellent as expected from the static experiments; however, as the interfacial structure becomes complicated (Figs. 4.8(b), (c), and (d)), the performance of the proposed sensor seems to be slightly reduced even though it still tracks the overall trend. According to Fig. 4.9, the time-averaged water level measurements from the impedance sensor well match those from the high speed camera, and for all cases the maximum deviation in time-averaged water level measurements between the sensor and the high-speed camera is roughly 0.037 which corresponds to about 1.48 mm in a pipe of diameter 40 mm.

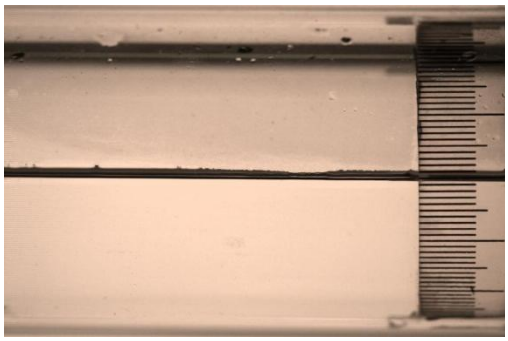

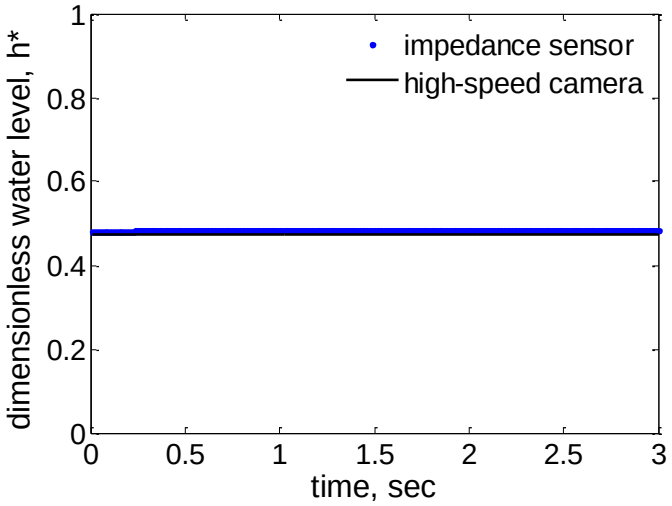

(a) j_ℓ = 0.03 and j_g = 0.0 m/s

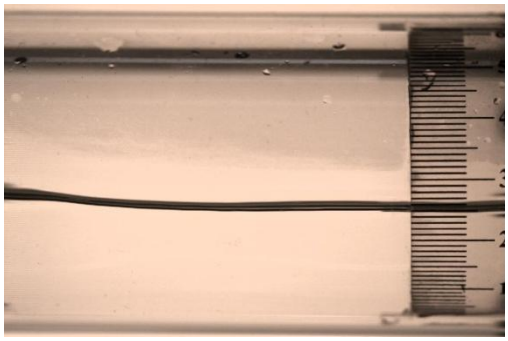

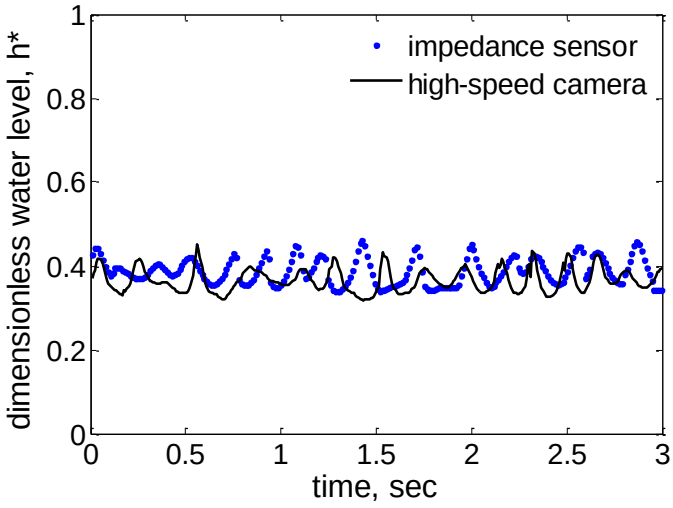

(b) j_ℓ = 0.06 and j_g = 1.5 m/s

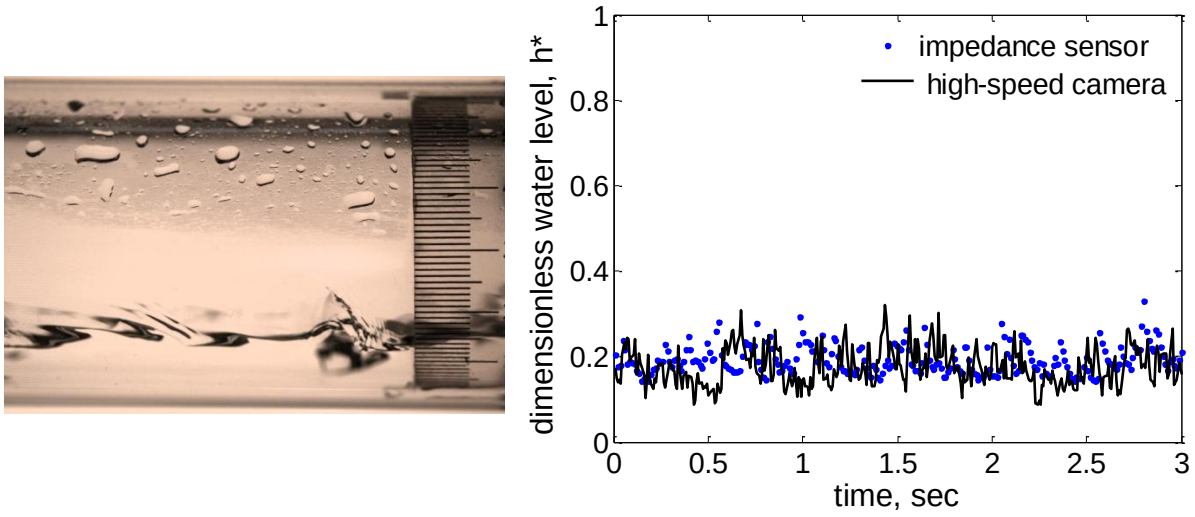

(c) j_ℓ = 0.06 and j_g = 8.0 m/s

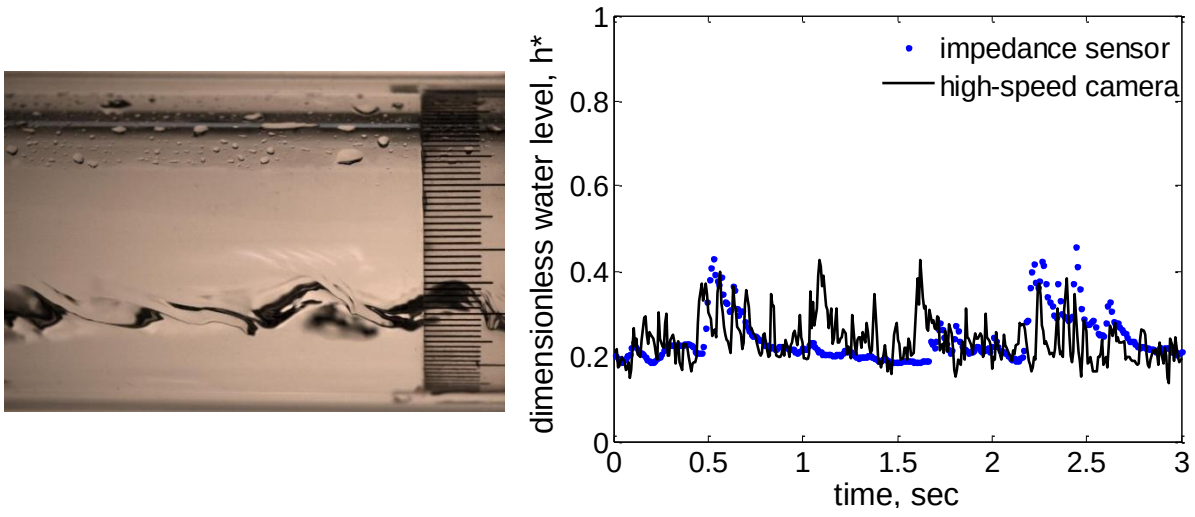

(d) j_ℓ = 0.09 and j_g = 6.0 m/s

Figure 4.8. Comparison of instantaneous water level measurements between the impedance sensor and the high-speed camera.

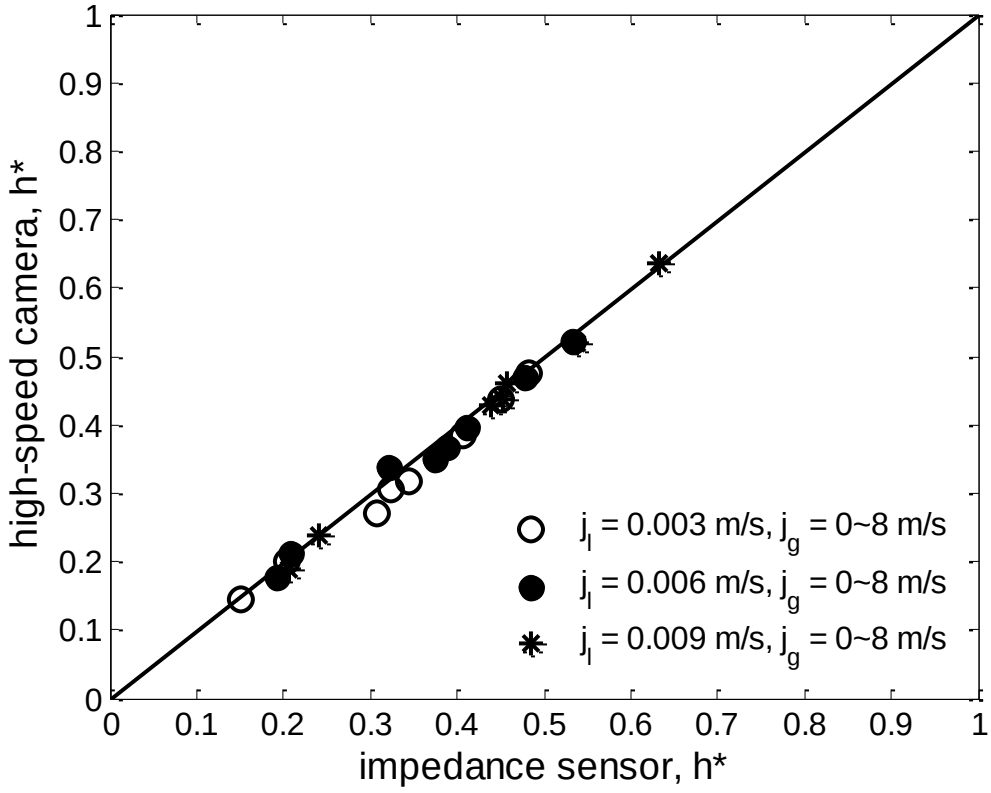

Figure 4.9. Comparison of time-averaged water level measurements between the impedance sensor and the high-speed camera.

4.5. Summary

In this chapter, several numerical simulations and experiments to determine the optimal sensor and gap sizes giving the linear response of all of the impedance, resistance and reactance to water level changes in air-water two-phase stratified flows were performed. The main conclusions are summarized as follows:

- The numerical study implied that the ring-type sensor with $W_e / D = 0.25$ and $W_g / D = 0.2$ gave the better performance (about 4.0 % relative error from ideal response) than others in view of the linearity and local measurement. The effect of

the signal frequencies on the sensor linearity were marginal.

- From the static experiments, when the proposed sensor configuration was used, the resistance, reactance and impedance showed good linear responses to the water level changes. The maximum deviation from the ideal linear response was 0.023 for the impedance in terms of the dimensionless water level and similarly those for the resistance and reactance cases were 0.036 and 0.029, respectively.
- For the dynamic experiments, the maximum deviation in the time-averaged water level measurements between the impedance sensor and high-speed camera was roughly 0.037 which corresponds to about 1.48 mm in a pipe of diameter 40 mm.

5. Electrical signal analyses on flow patterns of an inclined pipe

5.1. Flow patterns in near inclined pipes

The flow patterns in near-inclined pipes are mainly based on those in horizontal pipes. That is, the representative interfacial structures are classified into 4 groups: bubbly, stratified, intermittent and annular flows. Detailed characteristics of each flow pattern are given as follows:

- Bubbly flow

The gas bubbles are dispersed in the continuous liquid phase and bubbles generally exist in the upper part of the pipe due to their buoyancy. In horizontal or near-horizontal pipes this regime only occurs for high mass flow rates.

- Stratified flow

When the liquid and gas velocities are very low, complete separation of the two phases occurs. The gas phase exists in the top and the liquid in the bottom of the pipe and the interface has smooth or wavy structures.

- Intermittent flow

Further increase of the gas velocity causes interfacial waves to become large enough to wash the top of the pipe. This flow pattern is characterized by large amplitude waves periodically washing the top of the pipe. These large waves often contain entrained bubbles. The intermittent flow is sometimes classified into plug or slug flow patterns.

- Annular flow

For even larger gas flow rates, the waves on the interface are swept by the gas phase and the liquid exists around the pipe wall in the form of the film. Due to the gravity, the liquid film is thicker at the bottom than at the top. The interface between the liquid film and gas core is continually disturbed by small amplitude waves and droplets are dispersed in the gas core. When the mass flow rates are not enough to make stable film or the void fraction is high, the top of the pipe with thinner film becomes dry first so that the liquid film covers only some parts of the pipe wall and thus this is then classified as stratified wavy flow.

5.2. Conductance sensor

To analyze signal characteristics for the flow patterns in a downward inclined pipe, an electrical sensor was fabricated as shown in Fig. 5.1. Two concave plate-type electrodes are installed in the inner wall of the pipe and they are separated by $\delta \approx 0.09$ rad gap (about 2 mm for 45 mm inner diameter). Also, each electrode has 45 mm width for better sensitivity.

The electrical impedance was measured using the Hioki IM 3570 Impedance analyzer with the L2000 4-terminal probe. The applied voltage and frequency were set to 1 V and 10 kHz and in this frequency the contribution of the resistance to the impedance was over 99 %. That is, the sensor system is purely conductive.

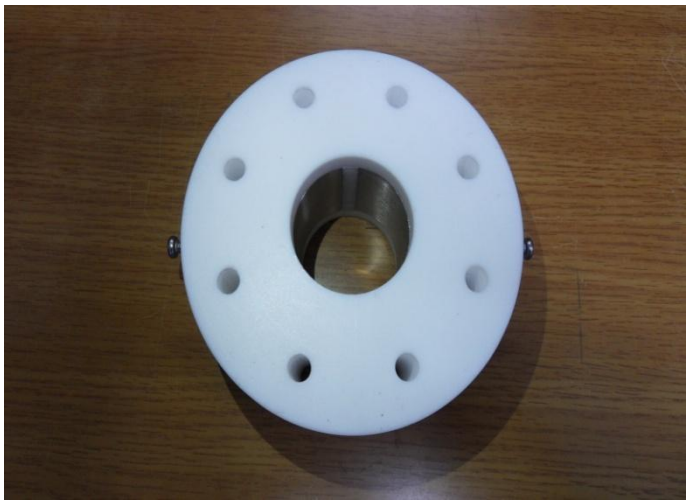

Figure 5.1. A conductance sensor for flow regime classification.

5.3. Experimental apparatus

Figure 5.2 shows a schematic of the experimental facility including an inclined test section. This facility mainly consists of 10 components as discussed in the preceding chapter (see Section 4.3): main collection tank, main pump with 5 HP, auxiliary pump with 3 HP, auxiliary tank, pre-heater with 20kW power, Coriolis water and air flow meters, compressor with 15 HP, inclined test section, and mixer. From the viewpoint of the flow, water in the main collection tank (I) is lifted by the main pump (II). This pumped water flows through the pre-heater (III) and the Coriolis water flow meter and then flows into the entrance of the test section. Similarly, air from the compressor flows through the Coriolis air flow meter and then it is injected to the air entrance (VII). These two fluids are finally combined in the mixer (IX) and flow into the test section (V) together. As shown in Fig. 5.2 and 5.3, the test section consists of two inclined pipes, two 87˚ bends with 267 mm curvature radii which connect the inclined pipes with the entrance and the auxiliary tank, and a 174˚ bend with 267 mm

curvature radius. The inner diameters of the inclined pipes are 45 mm and their lengths from the end of the 87˚ bend to 174˚ bend are about 3200 mm. The inclination angles are 3˚. These dimensions are approximately equal to those of the condensation heat exchanger for the PAFS designed by Korea Atomic Energy Research Institute (KAERI).

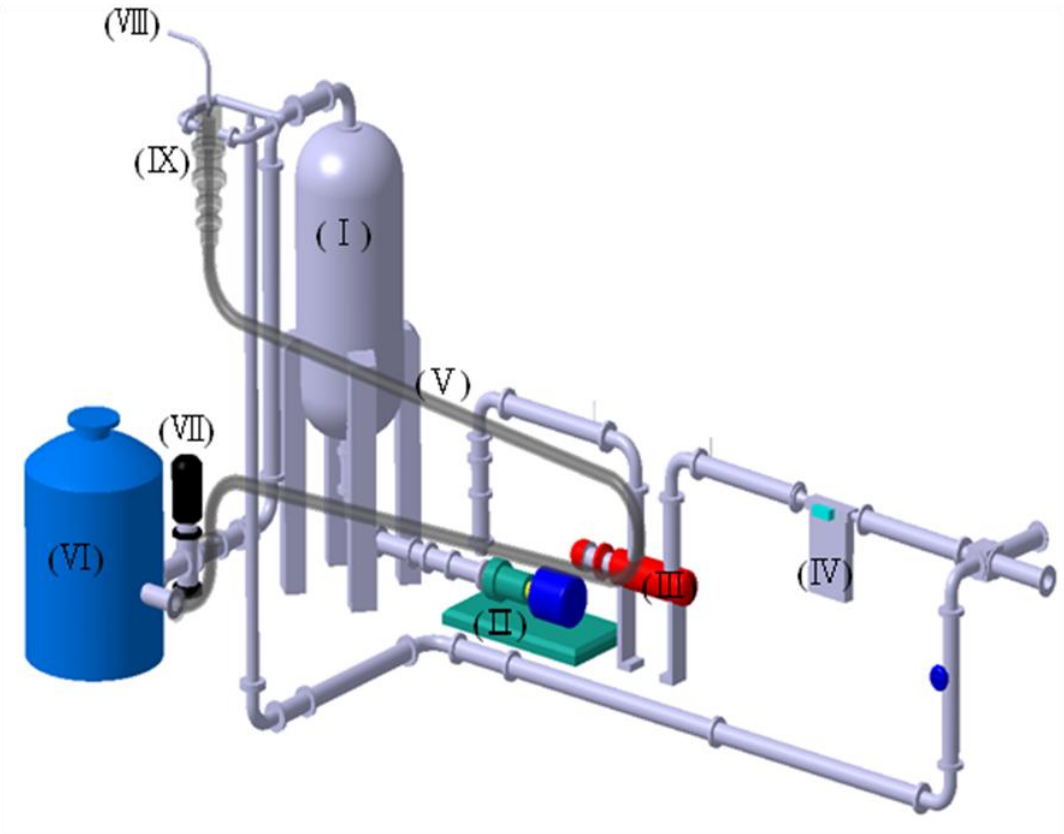

Figure 5.2. A schematic of an experimental apparatus.

Figure 5.3. A photograph of a test section.

5.4. Signal characteristic for various flow patterns

The conductance sensor was installed in the position roughly 2.5 m away from the end of the 87˚ bend to reduce the entrance effect. The superficial velocities ranging from 0.29 to 2.7 m/s for water and those from 0.2 to 21.0 m/s for air were applied. These flow conditions are illustrated with corresponding flow patterns in a theoretical flow regime model as shown in Fig. 5.4. In this figure, each colored circle and rectangle represent the flow conditions and the solid line is the flow regime transition boundary of the Taitel and Dukler's theoretical model (1976) given in Appendix.

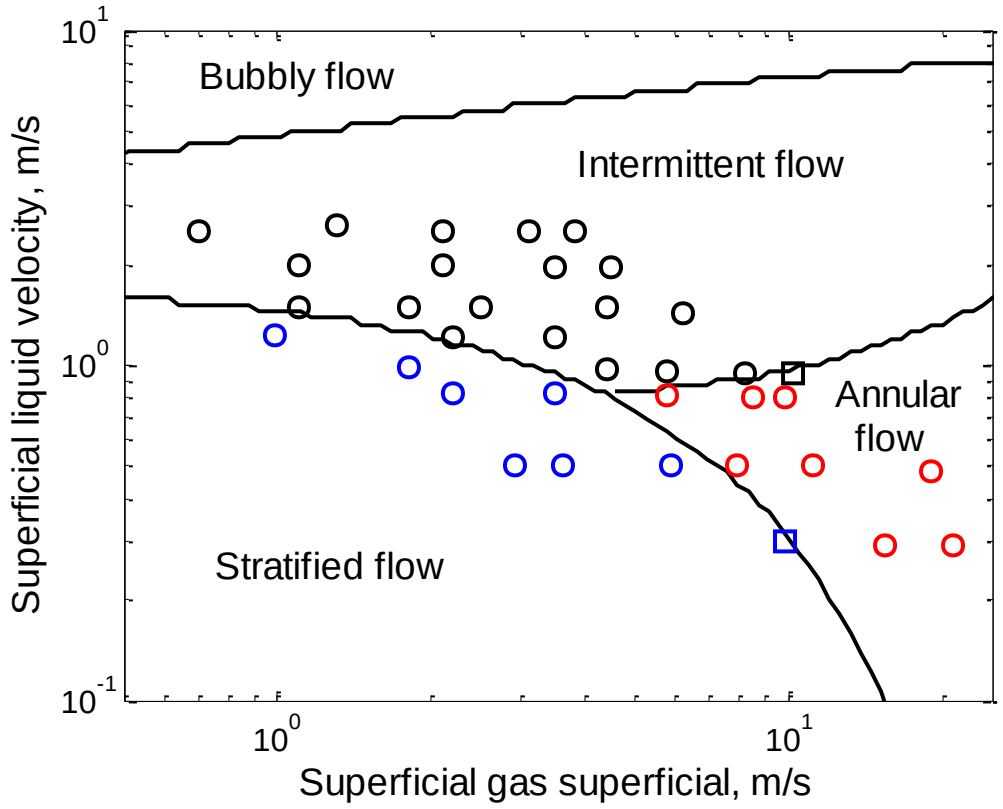

Figure 5.4. Flow conditions and corresponding flow regimes
(solid line: theoretical flow regime boundary, symbols: flow conditions).

For each flow condition, the measured conductance signals G were made dimensionless with the conductance value for the sensor filled with only water G_ℓ. That is, $G^* = G / G_\ell$. Figures 5.5 ~ 5.7 show the dimensionless conductance for given time sequences, probability density function (PDF) and power spectral density (PSD) for typical flow regimes.

In a stratified flow pattern (Fig 5.5), an almost constant conductance signal is observed. The PDF has a sharp peak and thus a very small variance. The dominant peak of the PSD is very small and corresponding frequency is about 1.6 Hz. As the gas flow rate increases, the waves grow and simultaneously some of them swept by the gas phase are present in the form of the liquid film around the wall of the pipe. The interface between the

liquid film and the gas core is continually disturbed by small amplitude waves. Due to these interfacial waves, the conductance signal significantly fluctuates (Fig. 5.6). Contrary to the stratified flow case, the PDF has a broad peak, indicating a large variance. The dominant peak of the PSD and corresponding frequency increases by 5 and 2 times larger, respectively.

As the liquid flow rate increases, the water level increases and even the liquid slugs appear (Fig. 5.7). Due to these liquid slugs, the conductance signal periodically goes up and down and the PDF has two peaks. One of them corresponds to the case where relatively stable water level maintains and the other indicates the liquid slugs. The dominant peak of the PSD shows more than 15 times larger value than the stratified flow case; however, the dominant frequency is comparable to the annular case.

Figure 5.8 shows the average values of the dimensionless conductance over the measurement time $\bar{G}^*$ and the variance Var_{G^*} for each flow condition. As expected before, in the case of stratified flows (blue circles in Fig. 5.8), the average values of the dimensionless conductance are widely distributed, but the variance are much less than other flow regimes ($\mathrm{Var}_{G^*} = 10^{-5} \sim 10^{-4}$). For intermittent and annular flows, the variance values are comparable even though those for the intermittent flows are somewhat larger than the annular flows on the whole. The average values of the dimensionless conductance, however, show some differences. That is, in most cases of the intermittent flows $\bar{G}^*$ are more than 0.45 and even some reaches 0.7, while those for annular flow are less than 0.45.

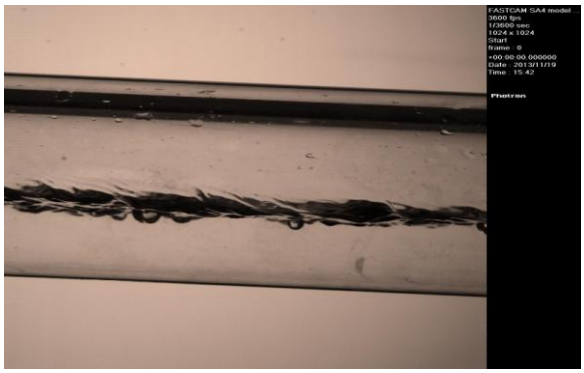

(a) Image

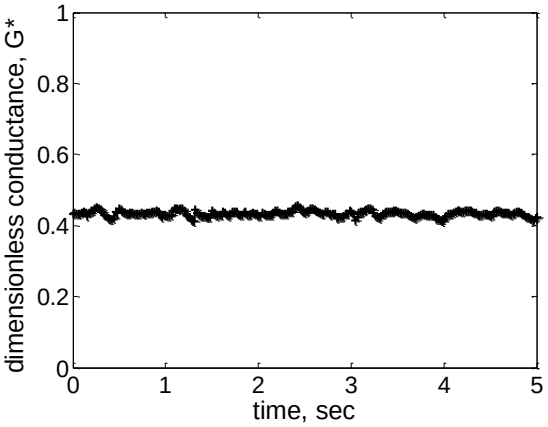

(b) G* for measurement time

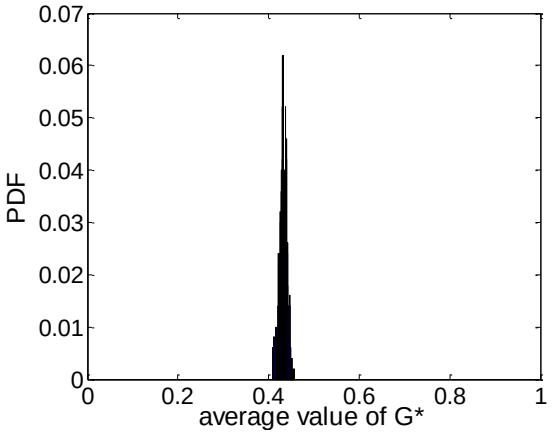

(c) PDF

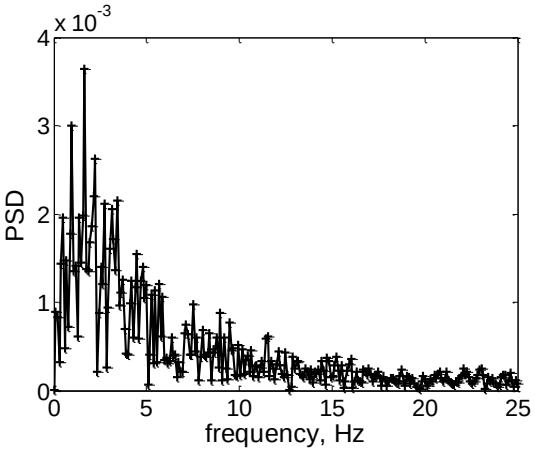

(d) PSD

Figure 5.5. Electrical signal characteristics for a stratified flow.

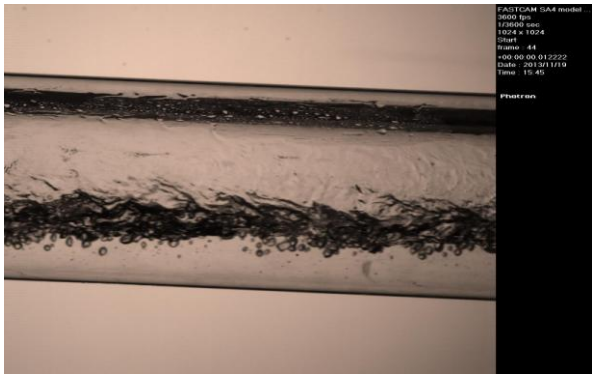

(a) Image

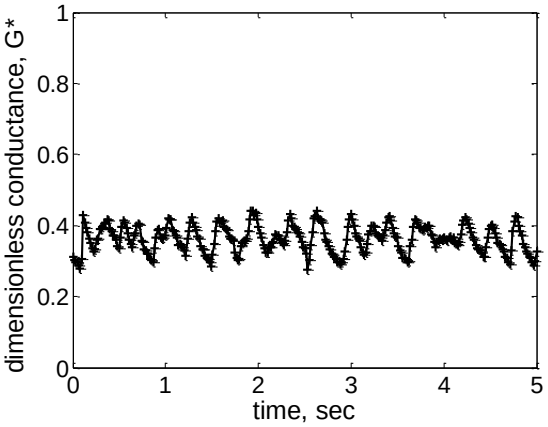

(b) G* for measurement time

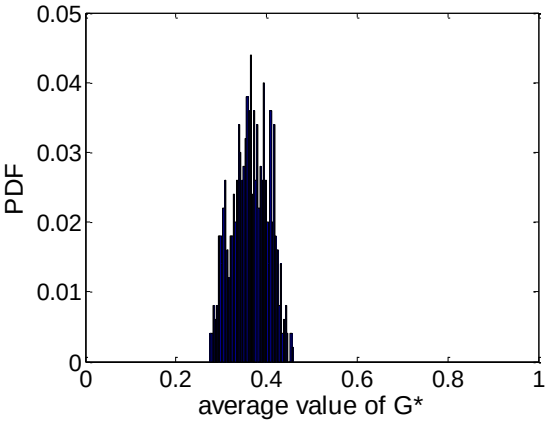

(c) PDF

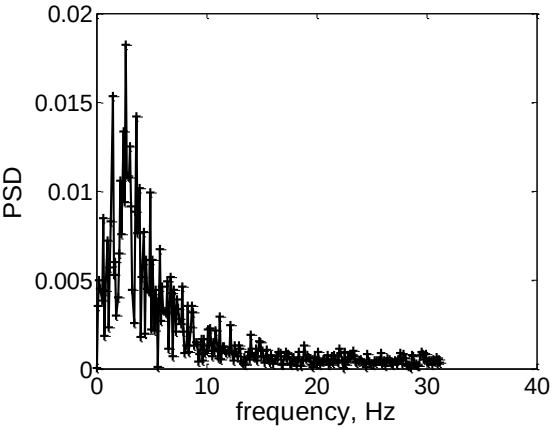

(d) PSD

Figure 5.6. Electrical signal characteristics for an annular flow.

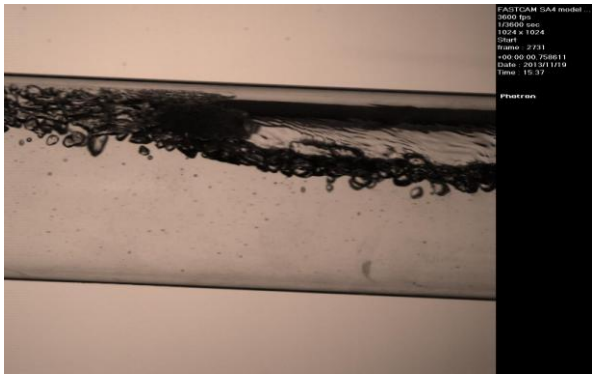

(a) Image

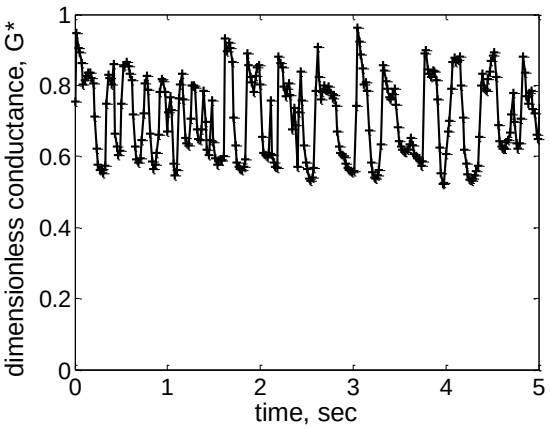

(b) G* for measurement time

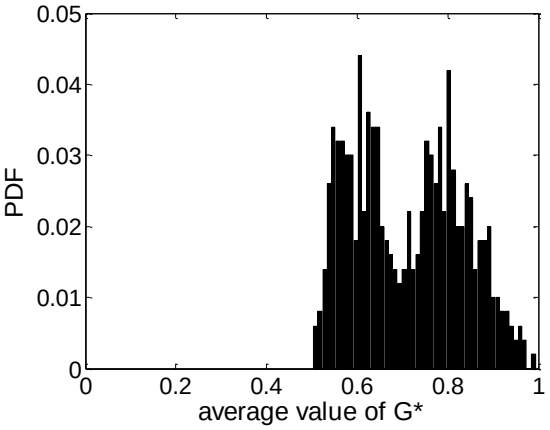

(c) PDF

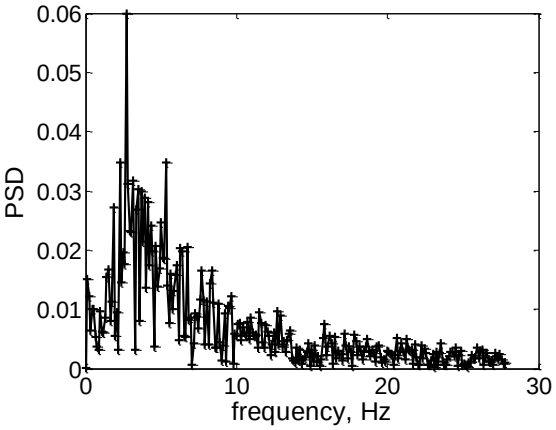

(d) PSD

Figure 5.7. Electrical signal characteristics for an intermittent flow.

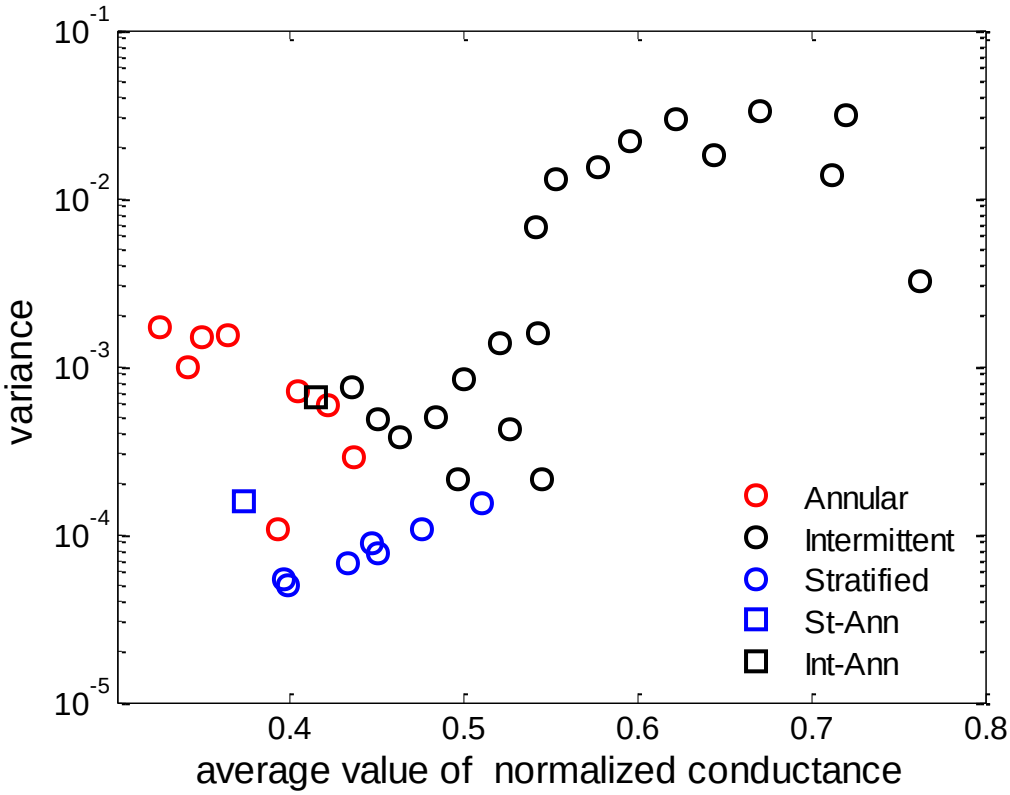

Figure 5.8. Average and variance values of G^* for various flow conditions.

5.5. Summary

In this chapter, electrical signal characteristics for various flow rate conditions which cover stratified, intermittent and annular flows were investigated. The main conclusions are summarized as follows:

- In the case of the stratified flows, the variance values had roughly $10^{-5} \sim 10^{-4}$ order, while for the annular flows they had ten to hundred times larger values than the stratified flow cases ($\mathrm{Var}_{G^*} = 10^{-4} \sim 10^{-3}$). These trends were also observed near the transition boundary between the stratified and intermittent flows.

- For the transition boundary between intermittent and annular flows, there were no big differences in variance values. However, the average values of the dimensionless conductance showed remarkable differences. In the intermittent flows $\bar{G}^*$ were over 0.45 on the whole, while those in the annular flows were less than 0.45.

6. Conclusions

In this thesis, the design of the impedance sensors giving good characteristics for volume fraction measurement was mainly reported. For analyses, two common flow patterns, annular and stratified flows, and two conventional sensor types, plate- and ring-type impedance sensors, were considered. In the case of an annular flow application gas core fluctuations was selected as a design consideration and for a stratified flow case the sensor linearity for water level changes was focused. For the annular flow case, the numerical and experimental evidences indicated that the plate-type sensor with a sensor gap angle equal to about 1.0 rad and the ring-type sensor with a larger gap size gave the most reliable void fraction measurement irrespective of the gas core fluctuations. Similarly, for the stratified flow application the ring-type sensor whose sensor width-to-diameter ratio and gap width-to-diameter ratio are equal to 0.25 and 0.2 showed the best performance in terms of the linearity and local measurement.

Also, this work investigated conductance signal characteristics for various flow conditions which cover stratified, intermittent and annular flows in an inclined pipe. The experimental results showed that the variance values of fluctuated conductance signals for the intermittent and annular flows were overall more than 10 times larger than the stratified flows and their average values showed some differences such that these three different flow patterns might be separated based on the statistical parameters. The determination of the detailed criteria for flow regime transition in the inclined pipe would be an interesting topic for further work.

References

Abouelwafa M S A and Kendall E 1980 The use of capacitance sensors for phase percentage determination in multiphase pipelines *IEEE Trans. Instru. Meas.* **IM-29** 24-7.

Åbro E and Johansen G A 1999 Improved void fraction determination by means of multibeam gamma-ray attenuation measurements *Flow Meas. Instrum.* **10** 99-108.

Ahmed W H 2006 Capacitance sensors for void-fraction measurements and flow-pattern identification in air-oil two-phase flow *IEEE Sensors J.* **6** 1153-63.

Andreussi P, Di Donfrancesco A and Messia M 1988 An impedance method for the measurement of liquid hold-up in two-phase flow *Int. J. Multiph. Flow* **14** 777-85.

Barnea D, Shoham O and Taitel Y 1982 Flow pattern transition for vertical downward two phase flow *Chem. Eng. Sci.* **37** 741-4.

Barnea D 1986 Transition from annular flow and from dispersed bubble flow - Unified models for the whole range of pipe inclinations *Int. J. Multiph. Flow* **12** 733-44.

Canière H, T'Joen C, Willockx A and De Paepe M 2008 Capacitance signal analysis of horizontal two-phase flow in a small diameter tube *Exp. Therm. Fluid Sci.* **32** 892-904.

COMSOL A B 2008 AC/DC Module Reference Guide (http://www.comsol.com).

De Kerpel K, Ameel B, T'Joen C, Canière H and De Paepe M 2013 Flow regime based calibration of a capacitive void fraction sensor for small diameter tubes *Int. J. Refrig.* **36** 390-401.

Euh D J, Yun B J, Song C H, Kwon T S, Chung M K and Lee U C 2001 Development of the five-sensor conductivity probe method for the measurement of the interfacial area concentration *Nucl. Eng. Des.* **205** 35-51.

Fossa M 1998 Design and performance of a conductance probe for measuring the liquid fraction in two-phase gas-liquid flows *Flow Meas. Instrum.* **9** 103-9.

Geraets J J M and Borst J C 1988 A capacitance sensor for two-phase void fraction measurement and flow pattern identification *Int. J. Multiph. Flow* **14** 305-20.

Hibiki T and Ishii M 2000 One-group interfacial area transport of bubbly flows in vertical round tubes *Int. J. Heat Mass Transf.* **43** 2711-26.

Hua P, Woo E J, Webster J G and Tompkins W J 1993 Finite element modeling of electrode-skin contact impedance in electrical impedance tomography *IEEE Trans. Biomed. Eng.* **40** 335-43.

Jaworek A, Krupa A and Trela M 2004 Capacitance sensor for void fraction measurement in water/steam flows *Flow Meas. Instrum.* **15** 317-24.

Jung S H and Lee M H 2005 *Digital Image Processing Using MATLAB* (Seoul: Hongrung Publishing).

Kendoush A A and Sarkis Z A 1995 Improving the accuracy of the capacitance method for void fraction measurement *Exp. Therm. Fluid Sci.* **11** 321-6.

Kendoush A A and Sarkis Z A 2002 Void fraction measurement by X-ray absorption *Exp. Therm. Fluid Sci.* **25** 615-21.

Kim J R, Ahn Y C and Kim M H 2009a Measurement of void fraction and bubble speed of slug flow with three-ring conductance probes *Flow Meas. Instrum.* **20** 103-9.

Kim S, Lee J S, Kim K Y, Kang K H and Yun B J 2009b An approximate formula for the capacitance-void fraction relationship for annular flows *Meas. Sci. Technol.* **20** 125404.

Lowe D C and Rezkallah K S 1999 Flow regime identification in microgravity two-phase flows using void fraction signals *Int. J. Multiph. Flow* **17** 433-57.

Mandhane J M, Gregory G A and Aziz K 1974 A flow pattern map for gas-liquid flow in horizontal pipes *Int. J. Multiph. Flow* **1** 537-53.

Olerni C, Jia J and Wang M 2013 Measurement of air distribution and void fraction of an upwards air-water flow using electrical resistance tomography and a wire-mesh sensor *Meas. Sci. Technol.* **24** 035403.

Ovacik L and Jones O C 1998 Development of an electrical impedance computed tomographic two-phase flows analyzer USDOE Report DE-FG07-90ER13032.

Paranjape S, Ritchey S N and Garimella S V 2012 Electrical impedance-based void fraction measurement and flow regime identification in microchannel flows under adiabatic conditions *Int. J. Multiph. Flow* **42** 175-83.

Prasser H-M, Bottger A and Zschau J 1998 A new electrode-mesh tomograph for gas-liquid flows *Flow Meas. Instrum.* **9** 111-9.

Prasser H-M, Scholz D and Zippe C 2001 Bubble size measurement using wire-mesh sensors *Flow Meas. Instrum.* **12** 299-312.

Prasser H-M, Misawa M and Tiseanu I 2005 Comparison between wire-mesh sensor and ultra-fast X-ray tomograph for an air-water flow in a vertical pipe *Flow Meas. Instrum.* **16** 73-83.

Prasser H-M 2007 Evolution of interfacial area concentration in a vertical air-water flow measured by wire-mesh sensors *Nucl. Eng. Des.* **237** 1608-17.

Rosa E S, Flora B F and Souza M A S F 2012 Design and performance prediction of an impedance void meter applied to the petroleum industry *Meas. Sci. Technol.* **23** 055304.

Schlegel J P, Miwa S, Griffiths M, Hibiki T and Ishii M 2014 Development of impedance void meter for evaluation of flow symmetry *Ann. Nucl. Energy* **63** 525-32.

Shu M T, Weinberger C B and Lee Y H 1982 A simple capacitance sensor for void fraction measurement in two-phase flow *Ind. Eng. Chem. Fundam.* **21** 175-81.

Song C H, Chung M K and No H C 1998 Measurements of void fraction by an improved multi-channel conductance void meter *Nucl. Eng. Des.* **184** 269-85.

Stahl P and Rudolf von Rohr P 2004 On the accuracy of void fraction measurements by single-beam gamma-densitometry for gas-liquid two-phase flows in pipes *Exp. Therm. Fluid Sci.* **28** 533-44.

Strazza D, Demori M, Ferrari V and Poesio P 2011 Capacitance sensor for hold-up measurement in high-viscous-oil/conductive-water core-annular flows *Flow Meas. Instrum.* **22** 360-9.

Taitel Y and Dukler A E 1976 A model for predicting flow regime transitions in horizontal and near horizontal gas-liquid flow *AICHE J.* **22** 47-55.

Todreas N E and Kazimi M S 1990 *Nuclear Systems: Thermal Hydraulic Fundamentals* Vol 1 (New York: Taylor and Francis).

Tsochatzidis N A, Karapantsios D K, Kostoglou M V and Karabelas A J 1992 A conductance probe for measuring liquid fraction in pipes and packed beds *Int. J. Multiph. Flow* **18** 653-67.

Vejražka J, Večeř M, Orvalho S, Sechet P, Ruzicka M C and Cartellier A 2010 Measurement accuracy of a mono-fiber optical probe in a bubbly flow *Int. J. Multiph. Flow* **36** 533-48.

Woldesemayat M A and Ghajar A J 2007 Comparison of void fraction correlations for different flow patterns in horizontal and upward inclined pipes *Int. J. Multiph. Flow* **33** 347-70.

국 문 초 록

이상유동은 화학, 석유, 원자력 산업 등과 같은 다양한 공학 분야에서 빈번히 관찰되는 현상이다. 특히, 이상유동 시스템에서 부피분율은 이상혼합밀도 및 점도, 평균속도, 압력강하, 그리고 열 전달 등과 같은 시스템 해석 및 설계와 관련된 여러 가지의 변수를 결정하는 중요한 역할을 한다. 이런 이유로, 퀵-클로징 밸브, 감마 또는 엑스레이 흡수, 광학 프로브, 그리고 전기 임피던스를 포함한 다양한 기법들이 부피분율 측정을 위해 제안되었다. 이 기법들 중, 특히, 전기 임피던스 기법은 쉬운 구현, 상대적으로 저렴한 비용, 빠른 데이터 취득속도, 비탐침성, 그리고 편리한 이동성과 같은 다양한 장점들을 갖는다.

전기 임피던스 기법은 두 상이 서로 다른 전기적 성질을 갖는다는 사실에 기반한다. 일반적으로, 전기 임피던스 기법에서 전압 또는 전류가 테스트 섹션에 설치된 전극으로 인가되고 유도된 전기저항 또는 정전용량의 측정 결과가 부피분율을 계측하는데 직접적으로 사용된다.

전기 임피던스를 이용하여 부피분율을 측정하는데 있어서, 센서의 전극 및 간극 크기는 센서 내부 전기장에 직접적으로 영향을 주기 때문에 가장 중요한 설계 변수들이다. 부적절한 센서 형상으로 인한 전기장의 불균일성은 부피분율에 대한 비선형 응답과 같은 바람직하지 못한 임피던스 센서 특성을 야기한다.

본 연구는 센서 형상에 대한 전기신호의 의존성을 고려하고 부피분율 또는 액막두께 측정에 유리한 특성을 제공하는 임피던스 센서를 설계하는 데

초점을 둔다. 이를 위해, 두 일반적인 센서 형상 (판형 및 링형)과 분리유동패턴 (층상류 및 환상류)을 고려한다. 환상류의 경우, 출력신호를 왜곡시킬 수 있는 기체코어의 요동을 중요 설계 변수로 고려하고 이런 요동의 영향 없이 안정한 기포율 측정을 제공하는 최적의 임피던스 센서 간극 크기를 결정한다. 유사하게, 층상류의 경우 링형 임피던스 센서의 전극 및 간극 크기를 액막두께 변화에 대한 선형성의 관점에서 최적화한다. 이와 더불어, 또 다른 응용분야로서 컨덕턴스 센서를 경사관 이상유동판별에 적용하고 다양한 유동조건에 대한 전기신호 특성을 해석한다.

Appendix. Taitel and Dukler's semi-theoretical flow regime model

A.1. Momentum balance for two-phase stratified flow

Let us consider a smooth stratified flow composed of the gas and liquid phases flowing through the pipe inclined by θ_{inc} as shown in Fig. A.1.

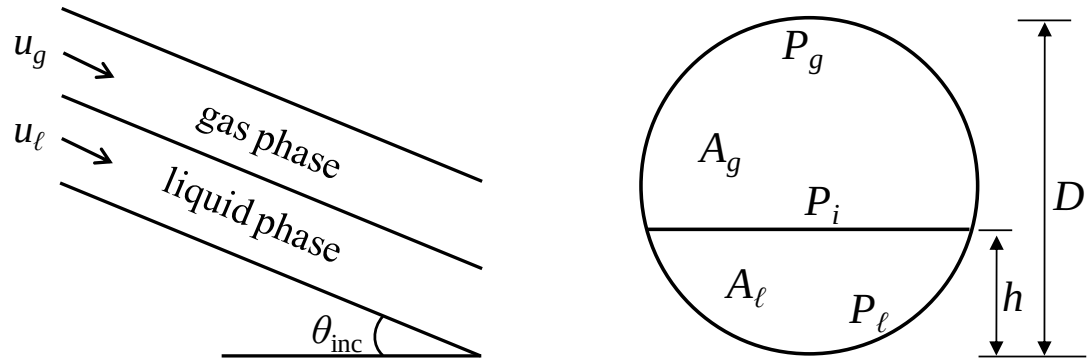

(a) Axial view (b) Cross-sectional view

Figure A.1. A stratified flow in an inclined pipe.

For steady-state flow, the momentum balances for each phase are

$$-A_\ell\left(\frac{dp}{dz}\right)-\tau_\ell P_\ell+\tau_i P_i+\rho_\ell A_\ell g\sin\theta_{\text{inc}}=0 \quad \text{for liquid phase,} \tag{A.1}$$

$$-A_g\left(\frac{dp}{dz}\right)-\tau_g P_g-\tau_i P_i+\rho_g A_g g\sin\theta_{\text{inc}}=0 \quad \text{for gas phase.} \tag{A.2}$$

Elimination of pressure gradient terms gives the momentum balance for two-phase flow that is,

$$\tau_g\frac{P_g}{A_g}-\tau_\ell\frac{P_\ell}{A_\ell}+\tau_i P_i\left(\frac{1}{A_\ell}+\frac{1}{A_g}\right)+\left(\rho_\ell-\rho_g\right)g\sin\theta_{\text{inc}}=0, \tag{A.3}$$

where the subscript 'g' ,'ℓ'', and 'i' denote the gas, liquid phase, and interface, respectively. The densities, cross-sectional areas and perimeters which each phase occupies are represented by ρ_ℓ, ρ_g, A_ℓ, A_g, P_ℓ, P_g, and P_i, respectively. The gravity acceleration is denoted by g. Here, the variables related to the flow geometry can be evaluated as follows.

$$A_\ell = \frac{1}{8} D^2 \left(\gamma - \sin \gamma \right) \text{ and } A_g = A - A_\ell, \tag{A.4}$$

$$P_\ell = \gamma \frac{D}{2} \text{ and } P_g = P - P_\ell, \tag{A.5}$$

where A and P is the cross-sectional area ($A = 0.25\pi D^2$) and the circumference ($P = \pi D$), respectively. In Eqs. (A.4) and (A.5), γ is given by $\gamma = 2\cos^{-1}\left(1 - 2h^*\right)$. Here, h^* is the dimensionless film thickness ($h^* = h / D$). Also, in Eq. (A.3) τ_ℓ, τ_g, and τ_i represent the liquid, gas, and interfacial wall shear stresses, respectively, which can be expressed in a conventional form as follows.

$$\tau_\ell = f_\ell \frac{1}{2} \rho_\ell u_\ell^2, \tag{A.6}$$

$$\tau_g = f_g \frac{1}{2} \rho_g u_g^2, \tag{A.7}$$

$$\tau_i = f_i \frac{1}{2} \rho_g \left(u_g - u_\ell \right)^2 \approx f_g \frac{1}{2} \rho_g u_g^2. \tag{A.8}$$

The approximation sign in Eq. (A.8) is established because the interfacial friction factor f_i is approximately equal to f_g and the flow transition occurs when $u_g \gg u_i$. The friction factors for turbulent flow are evaluated by the Blasius' expression as follows.

$$f_\ell = 0.046\left(\frac{D_\ell u_\ell}{\nu_\ell}\right)^{-0.2} \quad \text{and} \quad f_g = 0.046\left(\frac{D_g u_g}{\nu_g}\right)^{-0.2}, \tag{A.9}$$

where v_ℓ and v_g denote the kinematic viscosities of the liquid and gas phases, and also D_ℓ and D_g represent the hydraulic diameters for the liquid and gas phases, which are defined as

$$D_\ell = \frac{4A_\ell}{P_\ell} \quad \text{and} \quad D_g = \frac{4A_g}{P_g + P_i}. \tag{A.10}$$

A.2. Transition criteria

A.2.1. Transition from stratified to non-stratified flow

When the gas flows over a wave crest it accelerates and the pressure in the gas phase decreases due to the Bernoulli's effect, as a consequence, the wave grows. Meanwhile, the gravity force acting on the wave tends to attract the wave. If the pressure difference acting on the wave overwhelms the gravity force, the wave grows. Otherwise, the wave decays and the resultant flow pattern becomes stratified flow. That is,

$$p - p' > \left(h_g - h_g'\right)\left(\rho_\ell - \rho_g\right)g, \tag{A.11}$$

where h_g and h_g' are the thicknesses from the upper wall of the pipe to the smooth interface and to the wave crest, respectively. The variables p and p' represent the pressures acting on the smooth interface and the wave crest, respectively. Based on the Bernoulli's equation and continuity equation, Eq. (A.11) can be rewritten as

$$u_g > \left[2\left(h' - h\right)\left(\frac{\rho_\ell - \rho_g}{\rho_g}\right)g\cos\theta_{\text{inc}}\frac{A_g'^2}{A_g^2 - A_g'^2}\right]^{0.5}, \tag{A.12}$$

where $h = D - h_g$ and $h' = D - h_g'$. By taking Taylor expansion of A_g' about A_g we obtain the final expression for the transition boundary between stratified and non-stratified flow as follows.

$$u_g > C\left[\frac{\left(\rho_\ell - \rho_g\right) g \cos\theta_{\text{inc}} A_g}{\rho_g dA_\ell / dh}\right]^{0.5}, \tag{A.13}$$

where the coefficient $C = 1 - h^*$ and the differentiation dA_ℓ / dh is given by

$$\frac{dA_\ell}{dh} = \frac{0.25\left(D - \cos\gamma\right)}{\left[h^*\left(1 - h^*\right)\right]^{0.5}}. \tag{A.14}$$

A.2.2. Transition from annular to intermittent

A stable slug is formed when the liquid hold-up is sufficiently large to maintain such a slug. In the case that the liquid hold-up is not enough, the wave is swept up around the wall, as a consequence, annular flow occurs. This suggests that the transition between intermittent and annular flow strongly depends on the liquid hold-up or the liquid level. On the basis of this concept it was proposed that when the liquid level was above the centerline of the pipe ($h^* > 0.5$), intermittent flow occurred, otherwise, annular flow appeared.

A.2.3. Transition from intermittent to dispersed bubbly flow

It was suggested that the transition to dispersed bubbly flow occurred when the turbulent fluctuations overwhelmed the buoyant forces keeping the gas phase at the top of the pipe. The buoyant force for unit length of the gas phase is

$$F_{\text{buoy}} = g\cos\theta_{\text{inc}}\left(\rho_\ell - \rho_g\right)A_g. \tag{A.15}$$

The force due to the turbulent fluctuations is estimated by

$$F_{\text{turb}} = 0.5\rho_\ell \overline{u'^2} P_i, \tag{A.16}$$

where u' is the radial velocity whose root-mean square is equal to the friction velocity. That is,

$$\overline{u'^2}^{0.5} = u_* = u_\ell\left(f_\ell / 2\right)^{0.5}. \tag{A.17}$$

Because the transition occurs when $F_{\text{turb}} \geq F_{\text{buoy}}$, we get the final form for the transition boundary between intermittent and dispersed bubbly flow as follows.

$$u_\ell \geq \left[\frac{4A_g}{P_i}\frac{g\cos\theta_{\text{inc}}}{f_\ell}\left(1-\frac{\rho_g}{\rho_\ell}\right)\right]^{0.5}. \tag{A.18}$$

감사의 글

지난 5년 동안의 대학원 생활은 지식의 미천함 그리고 인성의 부족함을 깨닫기에 충분한 시간이었습니다. 학위논문을 마무리하는 이 글을 쓰며 돌아보니, 지나온 세월이 가슴 벅차게 다가옵니다. 너무나 많은 분들이 저에게 진심어린 관심과 도움을 주셨습니다. 모두 돌아보며 감사 인사를 드려야 하는데 그러하지 못함에 용서를 구합니다.

부족한 저를 제자로 받아드려, 하나에서 열 가지 가르침을 주시고, 물심양면 희생적 지원을 아낌없이 해주신 김 신 지도교수님께 진심으로 감사 드립니다. 연구적으로나 인간적으로 항상 모범적인 교수님의 모습을 거울삼아 제자로써 부끄럽지 않게 노력하며 살겠습니다. 또한, 석사 과정을 시작한 이래로 지금까지 한결같이 깊은 관심과 조언을 해주시는 김경연 교수님께 고개 숙여 감사 드립니다. 실험장치 설계에 헌신적으로 참여하시고 연구 과정 중 기술적인 조언을 아낌없이 해주신 부산대학교 윤병조 교수님께도 진심으로 감사 드립니다. 학사 과정부터 기본 소양을 잘 쌓을 수 있도록 지도해 주신 이윤준 교수님, 박재우 교수님, 이헌주 교수님, 천원기 교수님, 경희대학교 정범진 교수님, 김남진 교수님께 깊은 감사를 드립니다. 실험실에서 동고동락하며 저에게 헌신적인 도움을 주신 이보안 박사님, 굳은 일도 묵묵히 해준 실험실 식구들 영준, 승신, 성용, 바로, 우현, 동재, 문지영 선생님, 그리고 실험장치 설계와 연구논문 쓰는 데 늘 고심하는 이연건 박사님께 감사의 마음을 전합니다. 또한, 여러모로 많은 도움을 주신 김봉석 박사님, Dr. Khambampati, 그리고

실험장치 제작하는데 깊은 애정을 갖고 도움을 주신 김진홍 사장님 감사합니다. 에너지 공학과 대학원 선배 준호 형, 지훈 형, 승진 형, 동기 민국, 성식, 경욱, 성용이를 포함한 후배들에게도 감사의 마음을 전합니다.

칠순을 넘은 연세에 철 없는 자식 뒷바라지 하면서도 그 일이 항상 즐거우신 아버지 그리고 어머니, 항상 뒤에서 물심양면으로 지원해 준 형, 누나, 매형, 형수 그리고 가족 모두에게 감사를 드립니다. 석사 입학할 때 만나 긴 시간 동안 정말 힘들었을 텐데 불평 한 번 없이 응원해준 미숙에게 감사의 마음을 전합니다. 이 논문을 존경하고 사랑하는 자식바보 부모님께 바칩니다.